SCINTILLATION EFFECTS ON GPS SIGNAL AND TEC MODEL BASED ON NEURAL NETWORK

PHAM LE HOAI PHONG

A THESIS SUBMITTED IN PARTIAL FULFILLMENT
OF THE REQUIREMENT FOR THE DEGREE OF
MASTER OF ENGINEERING IN COMPUTER ENGINEERING
INTERNATIONAL COLLEGE
KING MONGKUT'S INSTITUTE OF TECHNOLOGY LADKRABANG
2012

KMITL-2012-IC-M-006-001

SCINTILLATION EFFECTS ON GPS SIGNAL AND TEC MODEL BASED ON NEURAL NETWORK

PHAM LE HOAI PHONG

A THESIS SUBMITTED IN PARTIAL FULFILLMENT

OF THE REQUIREMENT FOR THE DEGREE OF

MASTER OF ENGINEERING IN COMPUTER ENGINEERING

INTERNATIONAL COLLEGE

KING MONGKUT'S INSTITUTE OF TECHNOLOGY LADKRABANG

2012

COPYRIGHT 2012

INTERNATIONAL COLLEGE

KING MONGKUT'S INSTITUTE OF TECHNOLOGY LADKRABANG

Thesis Title	Scintillation Effects on GPS Signal and TEC Model Based on Neural Network
Student	Pham Le Hoai Phong
Student ID.	53601154
Degree	Master of Engineering
Program	Computer Engineering
Year	2012
Thesis Advisor	Assoc. Prof. Dr. Pornchai Supnithi

ABSTRACT

The Earth's ionosphere is an ionized region with several irregularities which affect the radio wave propagation. The drastic variation of electron density along the ionosphere degrades the trans-ionospheric signal. Particularly, the GPS signal transmitted through the ionosphere can fluctuate in terms of phase and amplitude, so called scintillations phenomena. At the receiver, it may result in the loss-of-lock and loss of GPS signal in worst case. Since the availability, precision, and reliability of GPS signal are important to our daily life, the study of ionosphere and its effects on GPS signal is necessary. In this thesis, we present the research work related to scintillations, loss-of-lock, and TEC modeling at Chumphon station, Thailand. An ionospheric scintillation monitoring is developed based on GPS software receiver. The results reveal that there are severe scintillations observed during the day with plasma bubble occurrence. On the other hand, the loss-of-lock is derived from GPS dual frequency receiver. As a result, it is evident that the L_2 frequency is more susceptible to the loss-of-lock events than the L_1 frequency. The loss-of-lock also illustrates a relationship with ROTI and the elevation angles. For TEC modeling, an improved neural network with extended input space is applied. The improved model gives better prediction of TEC for most of the months compared to the previous model.

ACKNOWLEDGEMENTS

First of all, I would like to express my sincere thanks to my supervisor, Assoc. Prof. Dr. Pornchai Supnithi. I am very much indebted to him for his guidance, patience and kindness. He not only supports my research study but also my student life during two years in Thailand. I am very fortunate being under his supervisor.

I would like to express my gratitude to every member of the Communications and Storage Research Group (CSRG) laboratory. Their friendship helps me overcome the difficulties of living abroad. It makes me feel our laboratory like a family.

I would like to acknowledge the lecturers and staffs in the International College, especially to Ms. .Arunee Suwanthan for her kind support during my study in Thailand.

My love is expressed to my family in Vietnam for their constant support, understanding and encouragement. I have been always full of energy for my study in their warm arms.

The financial support of this study was generously funded by the Japan International Cooperation Agency (JICA) under AUN/Seed-Net project. I would also like to warmly thank to the secretariats of the AUN/Seed-Net project who have always given helpful and kind support.

Bangkok, September, 2012

Pham Le Hoai Phong

TABLE OF CONTENTS

Page

LIST OF TABLES

Page

LIST OF FIGURES

Page

Chapter 1

Introduction

1.1 Motivations

Ionosphere is an ionized region of the Earth's atmosphere. The electron density in this region varies due to the effects of solar activities associated with geomagnetic field, leading to several ionospheric irregularities. Such the irregular ionosphere causes the radio wave signals scatter and delay. As a result, the ionosphere affects the satellite communications such as navigation satellites, broadcasting satellites, observation satellites, communications satellites, and others.

The Global Positioning System (GPS) is the first global navigation satellite system (GNSS) to be widely available for various civilian applications such as aeronautical navigation, surveying navigation, remote sensing, and geodesy. Since its applications have increasingly concerned with the human safety issue, the precision and reliability of GPS signal becomes important. The ionosphere with instability of electron density contributes apprehensive errors to positioning on GPS receiver.

In particular, scintillation phenomena created from ionospheric irregularities cause rapid fluctuations in amplitude and phase of GPS signal. At the receiver, scintillations result in attenuation/ reinforcement of signal intensity, phase noise, cycle slips, and loss-of-lock [1]. When the loss-of-lock occurs, the receiver cannot track the incoming signal due to the rapid fluctuation. The loss-of-lock potentially becomes the loss of signal in the worst case. Consequently, the communications between GPS satellite and receiver are disrupted for a while until the receiver can re-acquire the signal. Hence, it is essential to observe the scintillations as well as loss-of-lock in order to study their statistics, characteristics, and effects on GPS signal.

Total electron content (TEC) is one of the parameters which exhibit the characteristics of the ionosphere. The TEC varies over time, space, and the ionospheric irregularities. The ionospheric delay on GPS signals can be described in term of TEC. Moreover, the rate of TEC change index (ROTI) derived from TEC is frequently used for studying plasma bubble, which is the depletion region of electron density. When the plasma bubble occurs, the TEC rapidly

depletes (the ROTI significantly varies). It might result in scintillations and LOL occurrences. Hence, it is important to observe the TEC as well as develop a TEC model for prediction.

Thailand is located in the equatorial ionization anomaly (EIA) region where the TEC drastically fluctuates due to the ionospheric irregularities. Equatorial scintillations occur along this region. The severe scintillations can be frequently observed during equinox months and solar maximum period. Therefore, Thailand is an important location for ionospheric study and its effects on GPS signal, in general, and scintillation, loss-of-lock, and TEC studies, in particular.

In this research, all GPS data are collected at two stations in Thailand, a part of Southeast Asia Low-latitude Ionospheric Network (SEALION). This network is a collaboration between King Mongkut's Institute of Technology Ladkrabang (KMITL), Thailand; National Institute of Information and Communications Technology (NICT), Japan; Vietnam; Indonesia; Philippines; and China which contains several GPS-TEC receivers, GPS-scintillation receivers, ionosondes, all-sky imagers, and magnetometers, as shown in Fig. 1.1. Due to the available GPS data for recent years, there is a motivation to study ionosphere and its effects on GPS signal as well as develop a local model for TEC prediction. The GPS data at KMITL station are used for LOL study, while the GPS data at Chumphon station are used for scintillation study and TEC modeling.

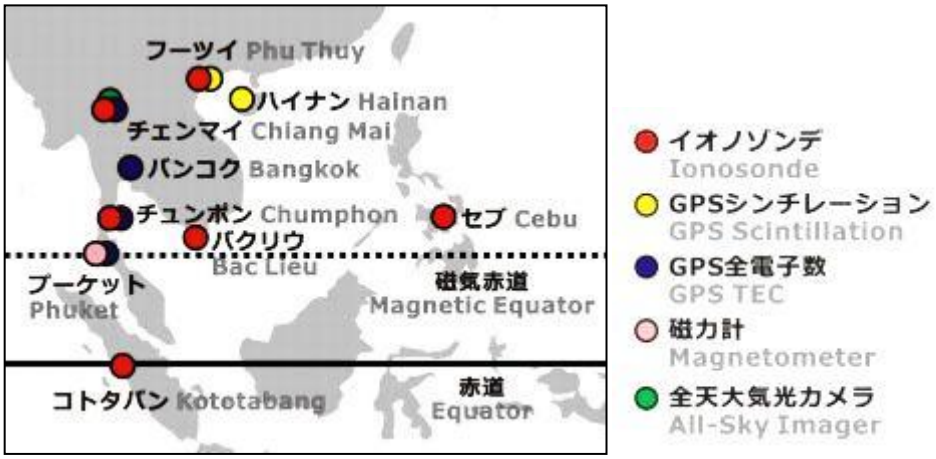

Figure 1.1: A map of SEALION network [2]

1.2 Objectives

This thesis presents three research topics that have been mentioned above including scintillations, loss-of-lock, and TEC modeling. The particular objectives of these topics are discussed as follows.

The first project is ionospheric scintillation monitoring using software GPS receiver at Chumphon station, Thailand. The purpose of this project is computing amplitude scintillations, S_4 index, from GPS signal using GPS software receiver at Chumphon station. The station contains a choke-ring antenna, a GPS L1 RF recorder, and a personal computer (PC). The recorder receives GPS RF signal and converts it into digitized intermediate frequency (DIF) data. Afterwards, the DIF data are processed on PC by GPS software receiver to calculate the in-phase (I) and quadrature (Q) signals. The S_4 index is finally obtained after detrending and ambient noise removal. We attempt to monitor the severe scintillations by selecting the observed periods with plasma bubble occurrence.

The second project is loss-of-lock statistics from the GPS receiver near Suvarnabhumi airport, Thailand. The purpose of this project is to study the loss-of-lock statistics from GPS signal using GPS dual- frequencies receiver at KMITL station. The loss-of-lock is determined based on the RINEX (Receiver Independent EXchange Format) file, a type of GPS data format. Then, the probability of loss-of-lock occurrences of the visible GPS satellites is computed. From these results, the loss-of-lock statistics and its relationship on ROTI and the elevation angle are investigated.

The third project is TEC modeling based on improved neural network over Chumphon station, Thailand. The purpose of this project is modeling the TEC for prediction based on neural network (NN) at Chumphon station. By utilizing the observed TEC data associated with solar activity and geomagnetic activity indices as the input of NN, the predicted TEC can be obtained as the output of the NN. The individual contribution of each input parameter to performance of the model is investigated. Afterwards, the improved model is compared to the previous model in 2007. Moreover, the predictability of the improved model also is tested in 2010.

1.3 Thesis Outline

This thesis is divided into seven chapters. Chapter 1 presents the motivations and objectives of this research. There are three research topics introduced with respect to scintillations, loss-of-lock, and TEC modeling.

The primary knowledge of ionosphere is given in Chapter 2. The ionosphere is presented as vertical structure of plasma density as well as latitudinal structure. The TEC variations depend on temporal and spatial variations, and ionospheric irregularities. The scintillations are characterized by amplitude scintillations and phase scintillations.

In Chapter 3, the Global Positioning System (GPS) is briefly explained in terms of GPS signal, positioning concept, and the operation of GPS receiver. It also shows how the TEC can be derived from GPS observations. The ionosphere presents its effects on GPS signal by group delay and phase advance.

Chapter 4 describes the ionospheric scintillation monitoring using software GPS receiver at Chumphon station, Thailand. The computation of S_4 index and the estimation of carrier-to-noise ratio are provided. The system is tested on selected periods with plasma bubble occurrence to observe the fluctuation of amplitude scintillations.

Chapter 5 describes the loss-of-lock statistics from the GPS receiver near Suvarnabhumi airport, Thailand. The methodology for determining loss-of-lock occurrences is given. Then the relationships of loss-of-lock with ROTI and the elevation angle are investigated.

Chapter 6 describes the TEC modeling based on improved neural network over Chumphon station, Thailand. The background of neural network and the structure of the improved neural network model are presented. Afterwards, the results of comparison between the improved neural network model and the previous one are discussed. The accuracy of predict TEC of the improved model is evaluated.

Finally, all the research works and future works are concluded in Chapter 7.

Chapter 2

Ionosphere

2.1 The definition of Ionosphere

2.1.1 Neutral Atmosphere

Neutral atmosphere is a region surrounding the Earth with the composition of various gases. It can be subdivided into a number of layers based on temperature in Kelvin (K) as shown in Fig. 2.1. The lowest and heaviest layer, troposphere, is from the surface of the Earth to about 10-km height. In this region, the temperature decreases with altitude due to the transmitted energy from the surface. The temperature reaches the minimum at the tropopause which is the upside boundary of this layer. The stratosphere extends from the tropopause to about 50-km height. Due to the solar ultraviolet (UV) absorption by ozone, the temperature starts to increase until reaching the maximum of around 270 K at stratopause. The upper layer, mesosphere, is considered the coldest region in the terrestrial atmosphere. The temperature of this layer declines with height and reaches the minimum value at mesopause. Above 100 km, the thermosphere is the hottest layer in the terrestrial atmosphere due to the solar UV and solar extreme ultraviolet (EUV) radiation. The temperature steady increases up to over 1000 K. In this layer, the free electrons can exist for a short period before combining to the positive ions. It is noted that these free electrons significantly affect radio waves propagating the neutral atmosphere.

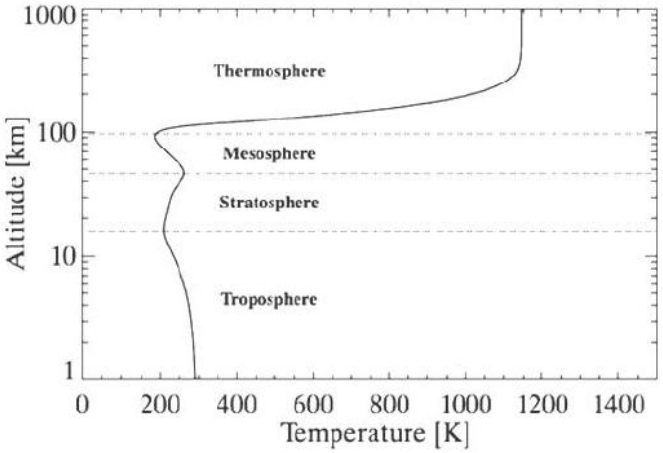

Figure 2.1: The temperature structure of the neural atmosphere [3].

2.1.2 Ionosphere

Under the solar radiation, the electrons are dislodged from the neutral gas atoms and molecules. The plasma including free electrons and ions varies with time, geographical location, and solar disturbances, which results in several irregularities affecting radio signal. Therefore, we define the ionized region of the upper neutral atmosphere as the Earth's ionosphere. Even though the upper and lower boundaries of the ionosphere are not well defined, for the most practical purposes, it can be roughly ranged at the altitudes of about 50-1000 km due to the distribution of plasma density. The ionosphere periodically varies with diurnal variation, seasonal variation as well as solar cycle variation. In addition, the ionospheric irregularities caused by solar disturbance travelling along the ionosphere and affect the Earth-space communications system.

2.2 The structure of the ionosphere

The solar radiation is differently absorbed at different layers of the neutral atmosphere due to the fact that its compositions vary with the altitude. Therefore, the ionosphere can be characterized as a vertical structure of plasma density as shown in Fig. 2.2. The ionosphere can be separated into several layers including D, E, and F layers based on the different levels of electron density. The peak of electron density usually occurs in F-layer which extends from about 150km to 500 km in height. The F-region is sub-divided into the F1 and F2 layers under the solar extreme ultraviolet (EUV) radiation during the day and re-combines at night. The below layer at the altitude of about 90-150 km is E-region formed by solar soft X-ray absorption. The electron density of this region decreases at night time. The D-region, extending from about 60 to 90 km above the Earth's surface, is affected by solar hard X-ray during day time and rapidly disappears at night.

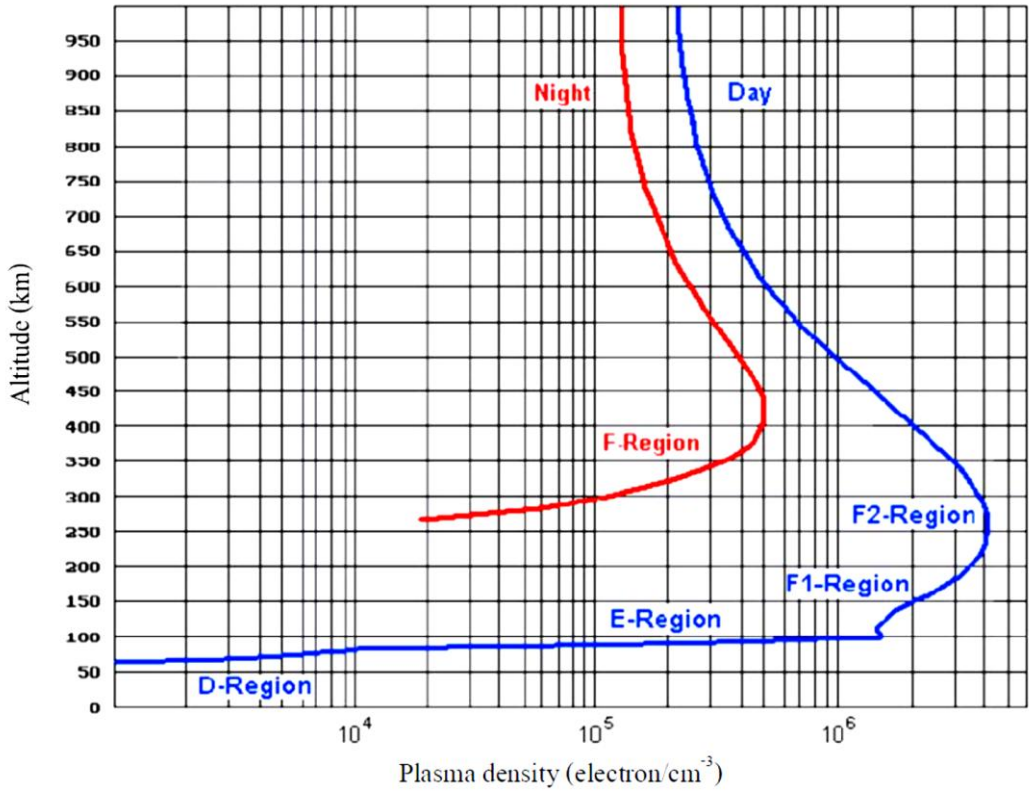

Figure 2.2: The vertical structure of the ionosphere [4].

The ionosphere can also be presented as a latitudinal structure including high-latitude, mid-latitude, and low-latitude regions. At high-latitudes, the ionospheric composition significantly depends on the electric field of magnetosphere and the auroral precipitation. The geomagnetic storms in auroral and polar cap regions can result in the irregularities of plasma density. At mid-latitudes, there is a high plasma density along the magnetic field due to effects of neutral wind, pressure gradient, gravity, and others. It results in plasma instabilities over this region. At low-latitudes, the plasma perpendicularly moves with the geomagnetic field. After sunset, the plasma flows upward due to $E \times B$ force formed by an eastward electric field. Then, the plasma is forced downward due to the pressure gradient and gravity. This procedure is known as "*fountain effect,* " as illustrated in Fig. 2.3, and creates a plasma enhancement region within $\pm 15^{\circ}$ latitudes from the magnetic equator, so called the "*equatorial ionization anomaly*" (EIA) [5].

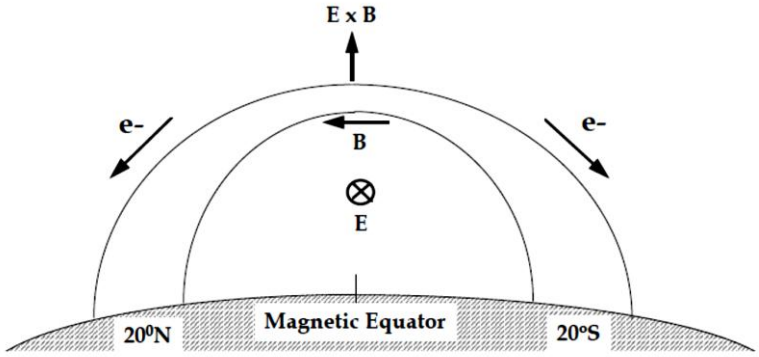

Figure 2.3: Illustration of the equatorial Fountain Effect (E and B represent the electric and magnetic field vectors, respectively) [6].

2.3 Total Electron Content

Total Electron Content (TEC) is one of the important parameters which can describe the plasma density of the ionosphere as well as the ionospheric instability that affects the radio wave of signal. The TEC is defined as a line integral of electron density along a signal ray path between a satellite and a receiver as follows:

$$TEC = \int_s N_e .ds \,, \tag{2.1}$$

where N_e is electron density ($electron.m^{-3}$), and s is a geometric range which is a straight line between the satellite and the receiver. The TEC is expressed in TEC units (TECU) with:

$$1TECU = 10^{16}\ electrons.m^{-2} \,. \tag{2.2}$$

The TEC values can be derived from GPS data and ionosonde data. The TEC values obtained from these methods are different because the GPS signals are transmitted from the altitude of about 22000 km to the ground, whereas the ionosonde transmits the signals from the ground up to a height of about 1000 km. In scope of this thesis, we focus on the TEC values derived from GPS data. There are two types of GPS-derived TEC including slant TEC and vertical TEC. The GPS-derived TEC can be obtained from code and carrier phase data of GPS signal. The details of GPS-derived TEC determination are described in Section 3.3.3.

The TEC is essential for studying the ionosphere and its effects on satellite communications. The TEC values follow the temporal and spatial variations of the electron

density in the ionosphere. The temporal variations of TEC can be separated into long-term variations and diurnal variations. For long-term variations, the TEC changes with the solar cycle and season. The solar cycle is a periodic variation of the solar radiation emitted from the Sun to the Earth. The period of a solar cycle is approximately 10.7 years based on the variation of sun spot number (SSN). The solar cycles from 1955 to 2012 are plotted in Fig. 2.4. The TEC values increase from a solar minimum to a solar maximum of the cycle. There are also seasonal variations of the TEC with high values during equinox months which are March and September and low values during solstice months which are June and December. For diurnal variations, the TEC reaches a maximum value during day time and a minimum value just before sunrise. The TEC also presents a large fluctuation from day to day.

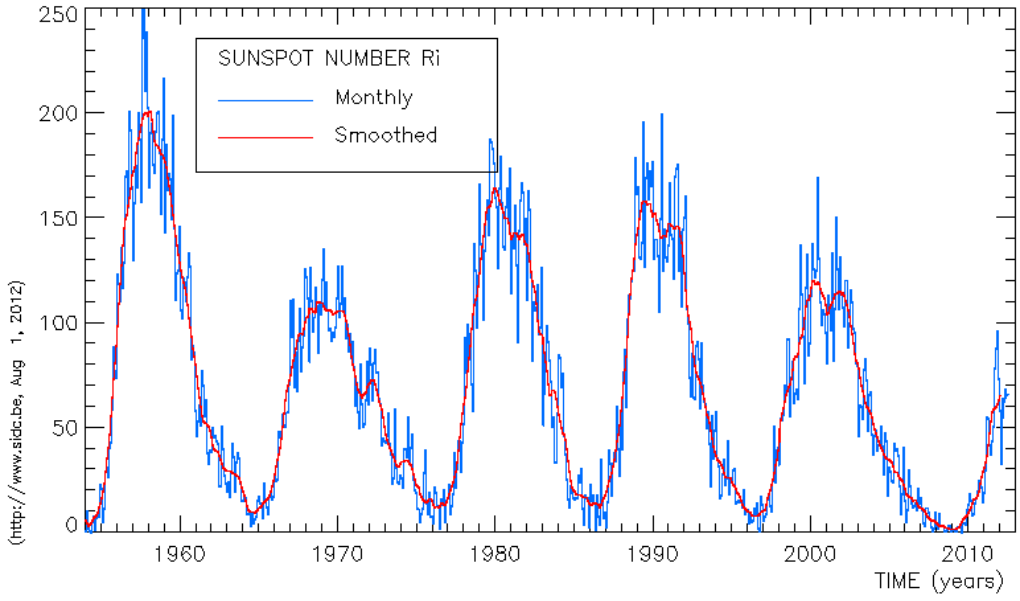

Figure 2.4: Solar Cycles from 1955-2012 [7].

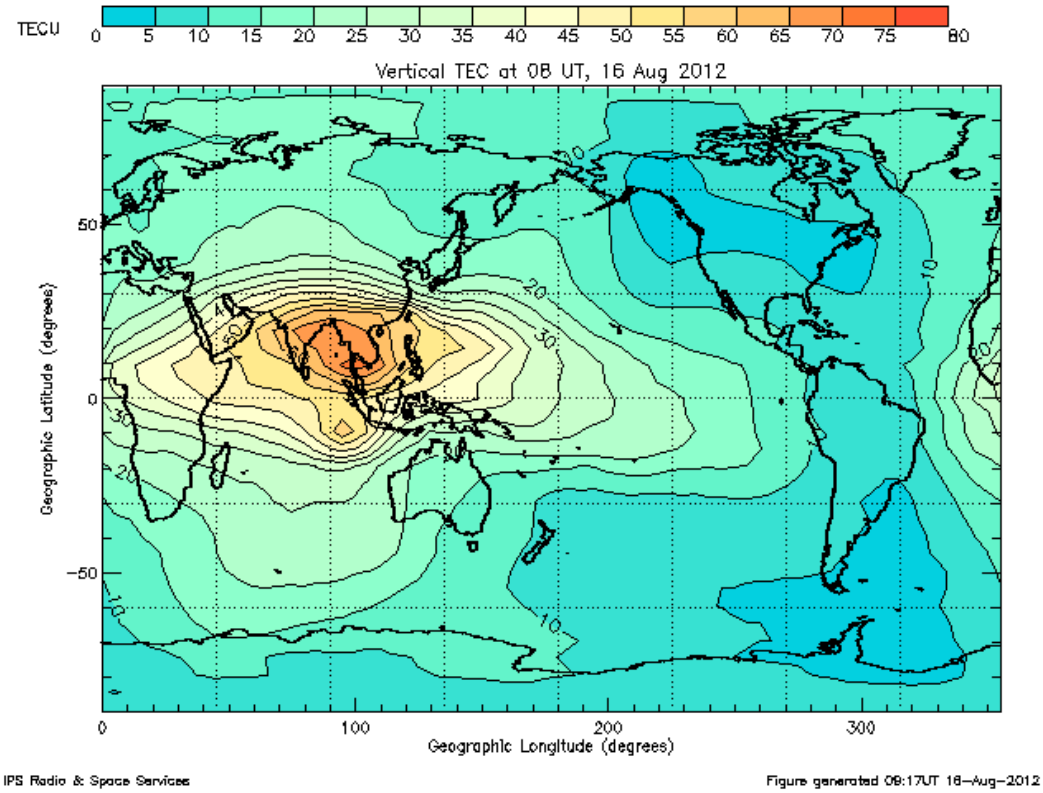

Figure 2.5: The map of TEC with spatial variations [8].

For spatial variations, the distribution of TEC levels is different for various regions around the Earth as shown in Fig. 2.5. One of the important regions, the "equatorial ionization anomaly" (EIA) region, is considered a significant feature of the low-latitude ionosphere with the high probability of drastic TEC-fluctuation. The EIA region covers the area within $\pm 15^{\circ}$ of latitude extending from the geomagnetic equator. Particularly, Thailand, located at EIA region, is an interesting location for ionospheric study and ionospheric effect on satellite communications.

Moreover, the TEC sporadically varies due to ionospheric irregularities. It can result in plasma bubbles in which the TEC immediately depletes. Plasma bubble occurrences can be explained by Rayleigh-Taylor instability. After the sunset, in the F-region, the re-combination of plasma in the lower layer is significantly faster than one in the upper layer. It produces the bubbles of low-density plasma which move upwards through a dense plasma region. Then, the plasma bubbles extend along the magnetic field line creating a horizontal scale of about over 200-km longitude and 1000-km latitude. Plasma bubbles tend to move eastward with velocities of about 50-200 m/s. The TEC inside the plasma bubble is depleted while the TEC at the edge of plasma bubble is dense. Consequently, the large TEC gradient can affect the radio wave

propagation. The transmitted signals through a plasma bubble rapidly vary in terms of phase and amplitude, known as ionospheric scintillation phenomena.

2.4 Ionospheric Scintillation

Ionospheric scintillations are sudden changes in terms of amplitude and phase of the radio signal propagating through the irregularities of ionosphere. It affects satellite communications and potentially interrupts the radio signal in the worst case. Scintillations primarily occur in the equatorial region within $\pm 20^{\circ}$ from the equator and in the auroral and polar cap regions. A sample of global map of scintillation pattern is shown in Fig. 2.6.

Auroral and polar cap scintillations are mostly produced by geomagnetic storms, whereas equatorial scintillations are due to the instabilities of electron density in F-layer and E-layer. Compared to the auroral and polar cap scintillations, the equatorial scintillations affect larger area of the Earth and their intensity is more severe. Moreover, the equatorial scintillations cover EIA region where the anomaly of electron density is significant. Particularly, Thailand, located in EIA region, is an interesting region for studying equatorial scintillations.

Equatorial scintillations are predominantly resulted from the irregularities in the F-layer during night time. After sunset, plasma bubbles are formed by the instabilities of electron density and disperse along the equatorial region. The strong electron-density gradients of plasma bubbles cause small-scale-ionospheric irregularities. These irregularities create a Fresnel diffraction which affects the amplitude and phase of radio wave, known as scintillation. On the other hand, scintillations can be produced by sporadic-E during day time as well. The sporadic-E is a thin layer of dense plasma in the E-layer at the altitude of about 100km. The steep plasma-density gradients of sporadic-E cause the scintillation occurrences.

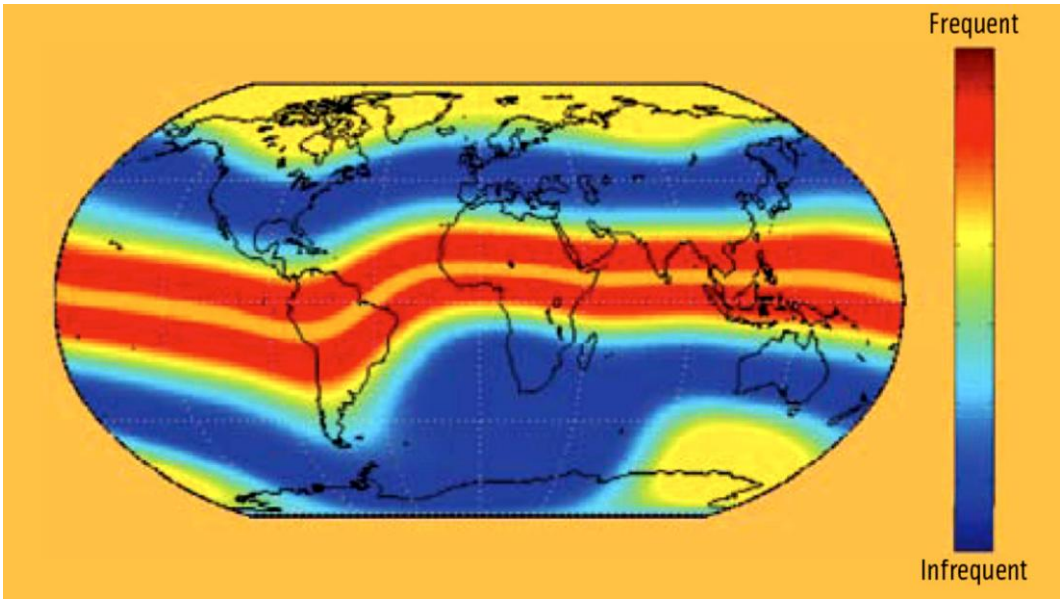

Figure 2.6: The global map of scintillation pattern [9].

Both types of scintillations including amplitude scintillations and phase scintillations are discussed as follows.

2.4.1 Amplitude scintillations

Amplitude scintillations cause the intensity of trans-ionospheric signals fluctuates rapidly. At receiver, strong amplitude scintillations can lead the intensity of incoming signals falling down below threshold of the lock-loop. In this case, the receiver must acquire the signal again. Amplitude scintillations are measured by $S4$ index which is the normalized standard deviation of signal intensity as follows:

$$S4 = \sqrt{\frac{E\left(SI^2\right) - E^2\left(SI\right)}{E^2\left(SI\right)}}, \tag{2.3}$$

where SI is signal intensity. The range of $S4$ index is between 0 and 1representing weak to strong scintillation.

2.4.2 Phase scintillations

Phase scintillations cause speedy fluctuations in carrier phase of trans-ionospheric signals. The fluctuations of carrier phase can be observed at the phase-lock-loop of the receiver. Phase scintillations result in phase noise, cycle slips, and loss-of-lock. The phase scintillations are observed from the standard deviation of carrier phase variation $\sigma_{\Delta\phi}$. The range of $\sigma_{\Delta\phi}$ index is between 0 and 1 radian.

Chapter 3

Global Positioning System

3.1 Global Positioning System

Global Positioning System (GPS), the first satellite based navigation system in the world, is developed and operated by the US Department of Defense. Its primary purpose is providing precise position, velocity, and time for defense applications. However, it has been recently available for civilian applications as well such as car navigation, tracking, survey, manufacturing, vessel voyage, and so on. Since GPS applications are widely used in our daily life, the precision and continuity of GPS navigation messages are significantly important.

The GPS system has three segments including a space segment, a control segment, and a user segment, as shown in Fig. 3.1. The space segment contains totally 32 satellites in six orbital planes at an altitude of about 20200km which consecutively transmit the navigation messages to the GPS receiver on dual L-band carrier signals including L_1 (1575.42 MHz) and L_2 (1227.60 MHz), respectively. The L5 frequency band (1176.45 MHz) has been recently added to be the third civil GPS signal which supports for the aeronautical navigation with improved availability and precision. There are at least four satellites are visible to a GPS receiver at anywhere and anytime on the Earth due to the distribution of the GPS constellation. This is an important issue required for the accurate positioning in the receiver. The control segment includes a master control station in US, four monitor stations and four ground antennas around the Earth. The control segment and space segment can communicate each other via S-band. Its duty is monitoring and controlling the operation of GPS satellites. The user segment is GPS receiver with several types applied in both military and civilian. It tracks the GPS signal and calculates position of the user.

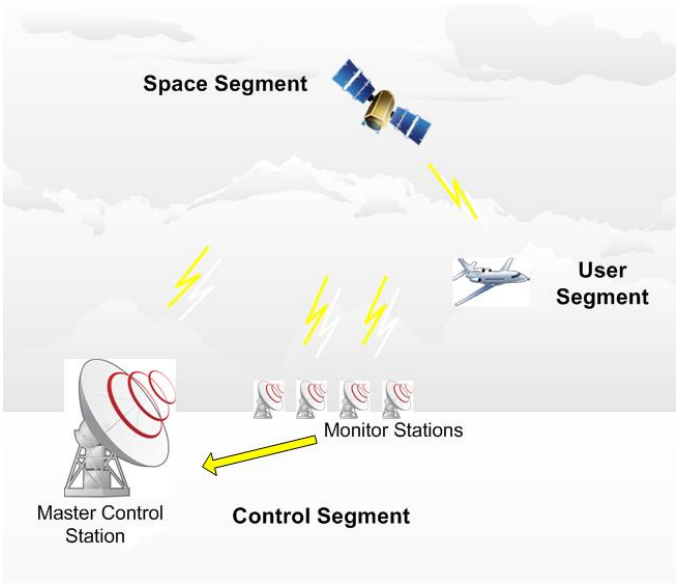

Figure 3.1: The scenario of GPS communications system.

GPS receivers spread wide range of cost and sophistication due to various military and civil applications. Almost the civil receivers with low cost can track only the L1 C/A signal. This kind of receiver is used for low-accuracy required applications such as car navigation, person tracking system, and so on. While the civil receivers which can track both L1 and L2 frequency, without the military P(Y) codes, provide a high accuracy. Hence, they are used for high-accuracy required applications such as surveying, science, aeronautical navigation, and so on. The military receivers which can track the P(Y) codes of both L1 and L2 are used for US army.

3.2 **The concept of positioning**

To calculate the position of GPS receiver, it is essential to require at least four GPS satellites which are simultaneously visible to the receiver, as shown in Fig 3.2. The three-dimensional position of the GPS receiver is computed by solving four range-measurement equations extracted from the navigation messages of four visible satellites at follows:

$$\begin{bmatrix} P^1 \\ P^2 \\ P^3 \\ P^4 \end{bmatrix} = \begin{bmatrix} |\left[x^{S1}, y^{S1}, z^{S1}\right] - \left[x^R, y^R, z^R\right]| + c(dt^R - dt^{S1}) + T^{S1} + I^{S1} + \varepsilon^{S1} \\ |\left[x^{S2}, y^{S2}, z^{S2}\right] - \left[x^R, y^R, z^R\right]| + c(dt^R - dt^{S2}) + T^{S2} + I^{S2} + \varepsilon^{S2} \\ |\left[x^{S3}, y^{S3}, z^{S3}\right] - \left[x^R, y^R, z^R\right]| + c(dt^R - dt^{S3}) + T^{S3} + I^{S3} + \varepsilon^{S3} \\ |\left[x^{S4}, y^{S4}, z^{S4}\right] - \left[x^R, y^R, z^R\right]| + c(dt^R - dt^{S4}) + T^{S4} + I^{S4} + \varepsilon^{S4} \end{bmatrix}$$

$$= \begin{bmatrix} \rho^1 + c\Delta t^{S1} + T^{S1} + I^{S1} + \varepsilon^{S1} \\ \rho^2 + c\Delta t^{S1} + T^{S2} + I^{S2} + \varepsilon^{S2} \\ \rho^3 + c\Delta t^{S3} + T^{S3} + I^{S3} + \varepsilon^{S3} \\ \rho^4 + c\Delta t^{S4} + T^{S4} + I^{S4} + \varepsilon^{S4} \end{bmatrix}, \qquad (3.1)$$

where $\left[x^{Si}, y^{Si}, z^{Si}\right]$ (for $i = 1:4$) and $\left[x^R, y^R, z^R\right]$ are the three-dimensional position vectors of the i^{th} satellite and GPS receiver, respectively, P^i and ρ^i are pseudorange and true range to the i^{th} satellite, respectively, c is the speed of light, dt^i and dt^{Si} are the receiver clock offset and the satellite clock offset, respectively, Δt^{Si} is the clock offset between the receiver and the satellite, T^{Si}, I^{Si}, and ε^{Si} are the tropospheric delay, the ionospheric delay, and the other error, respectively. The pseudorange measurement is based on the signal propagation delay from the GPS satellite to the receiver. It is described more detail in section 3.4.

The ephemerides derived from the navigation message provide the satellite position $\left[x^{Si}, y^{Si}, z^{Si}\right]$ and the satellite clock offset dt^{Si}.The T^{S1} and I^{S1} can be estimated from the priori models, whereas ε^{Si} can be minimized using least square method. Hence, there are four unknowns in four equations including the position of GPS receiver, $\left[x^{Si}, y^{Si}, z^{Si}\right]$, and the receiver clock offset, dt^{Si}. The accuracy of positioning mostly depends on the precise and reliable information of satellite's position and satellite's clock.

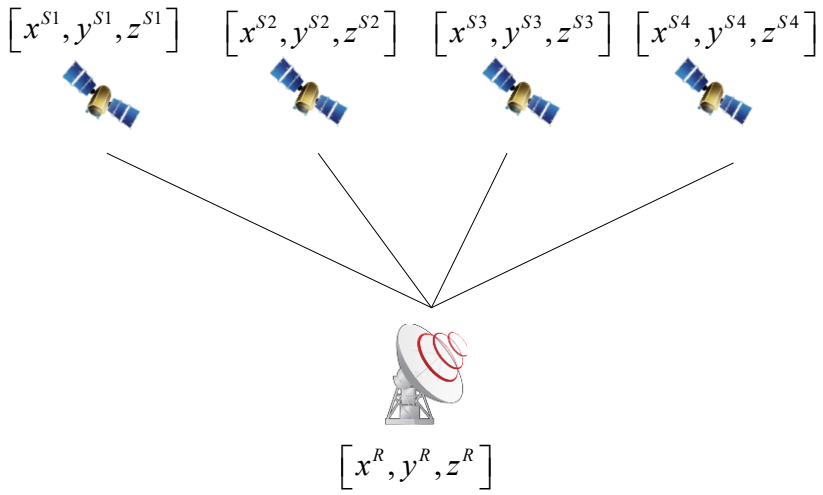

Figure 3.2: The positioning at GPS receiver and four visible GPS satellites.

3.3 GPS signals

The GPS signals are transmitted on two carrier frequencies of L-band, defined as L1 and L2. Both frequencies are derived from a common frequency, f_0 (10.23MHz), as follows:

$$\begin{aligned} f_{L1} &= 154 f_0 = 1575.42 \ MHz \ , \\ f_{L2} &= 120 f_0 = 1227.60 \ MHz \ . \end{aligned} \tag{3.2}$$

GPS signals are encoded using code division multiple access (CDMA) to allow all GPS satellites broadcast their signals on the common carrier frequencies. Each satellite has the unique spreading sequence of CDMA encoding. In short, the GPS signals are bi-phase modulated by spreading sequence and navigation message. An example of the GPS signal modulation is described in the Fig. 3.3.

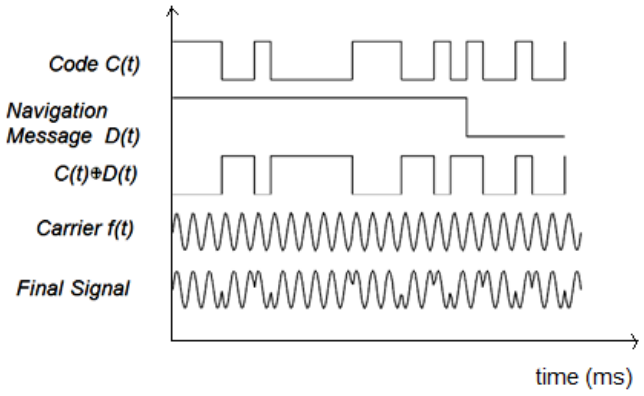

Figure 3.3: An example of the GPS signal modulation.

There are two unique spreading sequences or codes for each GPS satellite including the coarse acquisition code (C/A) and encrypted precision code (P(Y)). The C/A code contains 1023 chips (a chip is a bit that does not contain any information) with the chipping rate of 1.023MHz. The P code contains 23500 chips with the chipping rate of 10.23MHz. The C/A code is repeated every second whereas the P code is repeated every week at beginning of the GPS week. The C/A code is modulated only on the L1 carrier while the P(Y) code is modulated on both GPS carrier frequencies.

The navigation message is broadcast from a GPS satellite on L1 C/A and L2 P(Y) at the bit rate of 50 bps. Its data include the time of week, satellite clock, satellite orbit which enable the receiver to determine the satellite position and so far compute the receiver position.

In short, the transmitted GPS signals of k^{th} satellites on L1 and L2 frequencies are described as flowing equations:

$$\begin{aligned} s^k{}_{L1}(t) &= \sqrt{2P_{C1}}C^k(t)D^k(t)\cos(2\pi f_{L1}t) + \sqrt{2P_{P1}}P^k(t)D^k(t)\sin(2\pi f_{L1}t)\,, \\ s^k{}_{L2}(t) &= \sqrt{2P_{P2}}P^k(t)D^k(t)\sin(2\pi f_{L2}t)\,, \end{aligned} \tag{3.3}$$

where P_{C1}, P_{P1}, and P_{P2} are the signal powers in terms of C/A and P code, $C^k(t)$, $P^k(t)$, and $D^k(t)$ are C/A code, P(Y) code, and navigation data, respectively. The block diagram of GPS signal generation is illustrated in Fig 3.4.

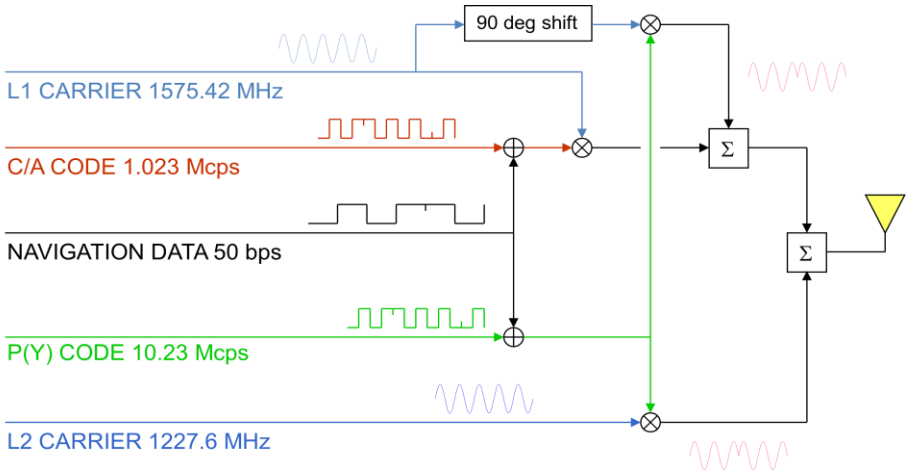

Figure 3.4: GPS signal generation at GPS satellite [10].

3.3 Group delay and phase advance

The phase velocity and group velocity of the GPS signal are defined as follows:

$$\begin{aligned} v_{ph} &= \lambda f \ , \\ v_{gr} &= -\frac{df}{d\lambda}\lambda^2 \ , \\ v_{gr} &= v_{ph} - \lambda \frac{dv_{ph}}{d\lambda} \ , \end{aligned} \tag{3.4}$$

where λ is the wave length and f is the frequency.

The ionosphere which is a dispersive medium affects the propagation of GPS signal. Therefore, the phase refractive index is presented by:

$$n_{ph} = 1 + \frac{c_2}{f^2} + \frac{c_3}{f^3} + \frac{c_4}{f^4} + ... \approx 1 + \frac{c_2}{f^2} \ , \tag{3.5}$$

where $c_i \ (i = 2,3,4,...)$ are the coefficients which do not depend on frequency but depend on the electron density along the propagation path of GPS signal. While the group refractive index can be approximated by:

$$n_{gr} \approx 1 - \frac{c_2}{f^2} \ . \tag{3.6}$$

The constant c_2 is estimated by Seeber [11] as $c_2 = -40.28 N_e \ [Hz^2]$. From (3.5) and (3.6), it is evident that $n_{gr} > n_{ph}$. Since the velocity is inversely proportional to the refractive index, it is obvious that $v_{gr} < v_{ph}$. As a result, the ionosphere causes the group delay and phase advance on GPS signal. It means that the GPS code measurements are delayed, and carrier phases are advanced. Both group delay and phase advance are accounted for the ionospheric delay which causes the error on GPS observations. The detail of GPS observations is presented in the next Section.

3.4 GPS observations

There are two types of GPS observations at the GPS receiver including pseudorange and carrier phase. The range measurement from the GPS satellites to the receiver can be estimated from these observations. The accuracy of both observations significantly depends not only on the internal system of satellite and receiver but also the environment such as ionosphere,

troposphere, and multipath. The pseudorange and carrier phase at both L1 and L2 frequencies are measured in range as follows.

3.4.1 Pseudorange observations:

$$P_1 = \rho + c\left(\tau_{P1}^{R} - \tau_{P1}^{S}\right) + I_{P1} + T + \varepsilon_{P1} \ ,$$
$$P_2 = \rho + c\left(\tau_{P2}^{R} - \tau_{P2}^{S}\right) + I_{P2} + T + \varepsilon_{P2} \ , \qquad (3.7)$$

where

P_1 : pseudorange measured on L1 frequency based on code

P_2 : pseudorange measured on L2 frequency based on code

ρ : geometrical range from satellite S to reciever R

τ^{R} : receiver clock error

τ^{S} : satellite clock error

T : tropospheric delay

$I_{P1/2}$: ionospheric delay in code measurement on L1/2

$\varepsilon_{P1/2}$: multipath delay, and other delay/error in code measurement on L1/2

3.4.2 Carrier phase observations:

$$L_1 = \rho - I_{P1} + T + \lambda_1 n_1 + \varepsilon_{L1} \ ,$$
$$L_2 = \rho - I_{P2} + T + \lambda_2 n_2 + \varepsilon_{L2} \ , \qquad (3.8)$$

where

L_1 : carrier phase measured on L1 frequency

L_2 : carrier phase measured on L2 frequency

ρ : geometrical range from satellite S to reciever R

δt^{R} : receiver clock error

δt^{S} : satellite clock error

T : tropospheric delay

$I_{P1/2}$: ionospheric delay in code measurement on L1/2

$\lambda_{1/2} n_{1/2}$: interger cycle ambiguities

$\varepsilon_{L1/2}$: multipath delay, and other delay/errors in carrier phase measurement on L1/2

The ionospheric delay is computed from the electron density along the propagation path of GPS signal and the carrier frequency as:

$$I = \frac{A}{f^2}\int_s N_e\, ds = \frac{A}{f^2} STEC\,, \tag{3.9}$$

where the constant A equals to 40.3.

3.5 GPS-derived TEC

The slant TEC ($STEC$) can be derived from both types of GPS observation including pseudorange and carrier code as follows:

$$\begin{aligned} TEC_P &= K(P_2 - P_1) \\ &= STEC + Kc[(\tau^S_{P2} - \tau^S_{P1}) + (\tau^R_{P2} - \tau^R_{P1})] + K(\varepsilon_{P2} - \varepsilon_{P1}), \\ TEC_L &= K(L_1 - L_2) \\ &= STEC + K(\lambda_1 n_1 - \lambda_2 n_2) + K(\varepsilon_{L1} - \varepsilon_{L2}) \end{aligned} \tag{3.10}$$

where the constant $K = \left[A(\frac{1}{f_2^2} - \frac{1}{f_1^2})(10^{16}) \right]^{-1} = 9.5196$ The terms $(\tau^S_{P2} - \tau^S_{P1})$ and $(\tau^R_{P2} - \tau^R_{P1})$ are satellite and receiver differential code bias (DCB), respectively, while the term $\lambda_1 n_1 - \lambda_2 n_2$ is phase ambiguity term.. The carrier phase is sensitive to the loss-of-lock of GPS signal which is a sudden change in the integer ambiguity including n_1 and n_2 caused by the ionospheric irregularities. Since the wavelengths of carriers are shorter than the lengths of codes, the $STEC$ derived from carrier phase is more precise than one from pseudorange. However, the phase ambiguity term is unknown for the receiver. Hence, the phase leveling which adjusts the TEC_L to be at the level of TEC_P is applied to eliminate the ambiguity offset. For instance, a simple phase leveling is adjusting the TEC_L to the mean value of the corresponding TEC_P.

The slant TEC can be converted into vertical TEC ($VTEC$). Assuming the ionosphere is a thin shell with a uniform electron density distribution. For Thailand region, the topside and bottom-side of the shell are assumed to be 600 km and 300 km of height, respectively [12]. The $VTEC$ is mapped on the ionospheric shell at assumed altitude of 400 km as:

$$VTEC = S(\varepsilon).STEC\,, \tag{3.11}$$

where the slant factor $S(\varepsilon)$ depends on the elevation angle of the signal ray path between GPS satellite and receiver ε as:

$$S(\varepsilon) = \frac{1}{\cos\left[\arcsin\left\{\frac{R}{R+h}\cos(\varepsilon)\right\}\right]} \quad , \tag{3.12}$$

where R and h are the radius of the Earth and the height of the satellite, respectively.

However, the thin shell model is not appropriate for the sophisticated structure of the ionosphere. Hence, it might cause the error of $VTEC$ estimation. The lower elevation angles are, the higher estimation errors become. Hence, only the data with the elevation angles higher than 45° should be utilized for TEC estimation in Thailand.

3.6 GPS receiver

The GPS signals are transmitted from GPS satellites to receivers through the ionosphere. The GPS signal of the k^{th} satellite at the receiver is a sum of the transmitted GPS signals on L1 and L2 frequencies as shown in (3.3), $s_{L1}^{k}(t)$ and $s_{L2}^{k}(t)$, as:

$$\begin{aligned} s^{k}(t) &= s_{L1}^{k}(t) + s_{L2}^{k}(t) \\ &= \sqrt{2P_{C1}}C^{k}(t)D^{k}(t)\cos(2\pi f_{L1}t) + \sqrt{2P_{P1}}P^{k}(t)D^{k}(t)y(t)\sin(2\pi f_{L1}t) \\ &\qquad + \sqrt{2P_{P2}}P^{k}(t)D^{k}(t)\sin(2\pi f_{L2}t) \end{aligned} \quad . \tag{3.13}$$

At front-end of the receiver, the GPS signal is sampled, down-converted to immediate frequency (IF), and converted from analog to digital. The output from the front-end is given as:

$$s^{k}[n] = C^{k}[n]D^{k}[n]\cos(\omega_{IF}n) + e[n] \quad , \tag{3.14}$$

where $e[n]$ is the noise.

Afterwards, the GPS signals are processed to extract the navigation message which is required for positioning. The GPS receiver is able to receive the signals from several GPS satellites simultaneously. Hence, it is necessary to identify which satellites are currently visible to receiver and allocate them into the channels. There are two methods for determining visible satellites including warm start and cold start. The warm start can reduce the time consuming of this process since it only uses the stored almanac data and the last position determined by the

receiver. However, if the receiver changes position or the almanac data is out of date, the information cannot be trusted leading to the imprecise determination of visible satellites. In these cases, the cold start is needed even though its process spends more time than the warm start. The cold start uses the acquisition method which checks the appearance of all satellites.

Generally, there are three steps for signal processing at GPS receiver including acquisition, tracking, and navigation data extraction. After that, the position can be calculated from pseudorange measurement and satellite's positions. Figure 3.5 shows the block diagram of the GPS receiver operation. The followings are detailed explanations of acquisition and tracking process.

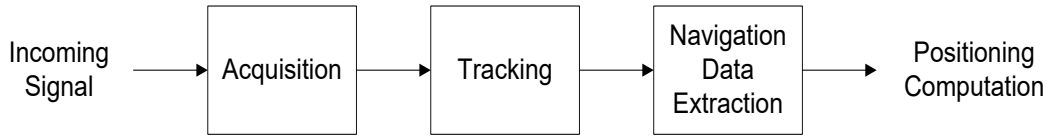

Figure 3.5: The overview of GPS receiver operation.

3.6.1 Acquisition

The acquisition aims at finding all visible GPS satellites with respect to the GPS receiver. Moreover, the acquisition also determines the coarse values of frequency and code phase of GPS signal for each visible GPS satellite. Even though all GPS signals are transmitted on the same carrier frequencies of L1 and L2, these carrier frequencies are shifted at the receiver due to the Doppler Effect. Hence, it is important to determine the frequency of GPS signal for decoding. On the other hand, the code phase is also needed for pointing out the beginning of C/A code in the current data block. The block diagram of acquisition is described in Fig. 3.6. The concept of acquisition is basically presented as follows.

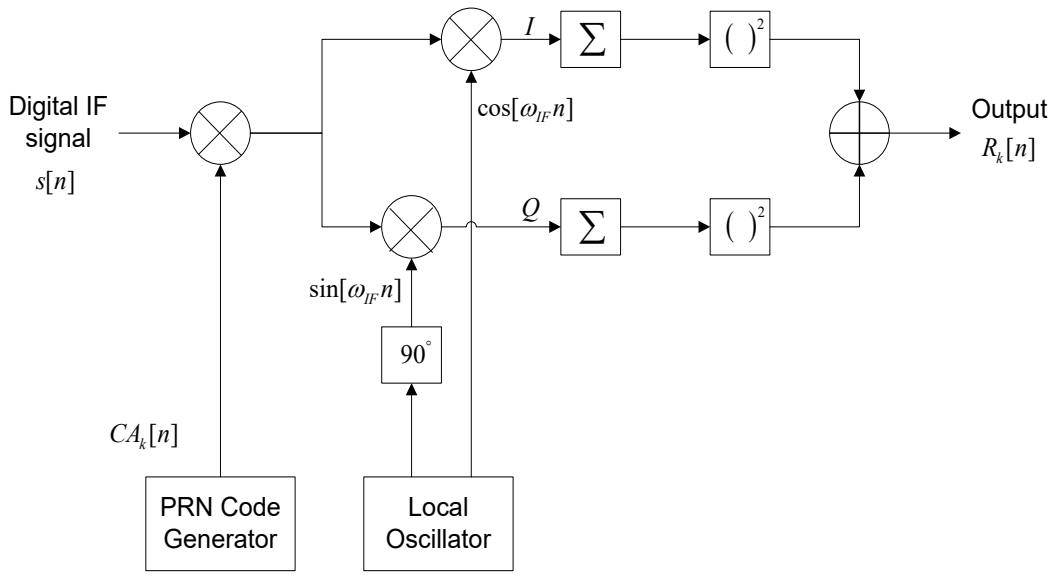

Figure 3.6: The block diagram of acquisition at GPS receiver.

At the GPS receiver, the digital IF signal $s[n]$ is written in terms of all incoming signals of all m visible satellites as:

$$s[n] = s^1[n] + s^2[n] + ... s^m[n]. \tag{3.13}$$

In order to acquire the k^{th} satellite, the C/A code of the k^{th} satellite, $CA_k[n]$, which is generated by the receiver is multiplied with the incoming signal $s[n]$. We notice that for all the C/A codes, there is nearly no cross correlation between each other, and there is nearly no autocorrelation with themselves except for zero lag. Therefore, only the incoming C/A code of k^{th} satellite has a high correlation with the generated C/A code at receiver, and only at zero lag. Only in this case, the C/A code can be removed from the incoming signal. The important point is that the generated C/A code must be aligned with the C/A code of incoming signal.

Afterwards, in order to remove the carrier wave of GPS signal, the signal is multiplied with a generated carrier wave and 90^0 phase shifts of the generated carrier wave, respectively. As a result, the in-phase (I) and quadrature (Q) signals are obtained. Then the I and Q components are accumulated and correlated to produce the correlator output, $R_k[n]$, as:

$$R_k[n] = \left(\sum_{n=1}^{L} s[n].CA_k[n].\cos[\omega_{IF}n] \right)^2 + \left(\sum_{n=1}^{L} s[n].CA_k[n].\sin[\omega_{IF}n] \right)^2, \tag{3.14}$$

where L is the length of one C/A code period and ω_{IF} is the radian frequency.

The Doppler Effect can probably cause the carrier frequency shifting up to $\pm 10\,kHz$ from the nominal frequency. Hence, it is necessary to search various frequencies along this range to find out the approximate frequency of incoming signal. With the proposed frequency step of $500\,Hz$, there are totally 41 searching points in this frequency range [13].

For each searching frequency, there are totally 1023 different code phases to be tried. Then, both I and Q signals for each case are squared and then summed up together. Their correlator output, $R_k[n]$, will be compared to each other as well as a threshold. The combination of code phase and frequency which has maximum value and exceeds the threshold is the correct one for k^{th} satellite. An example of acquisition results for a visible satellite is illustrated in Fig. 3.7.

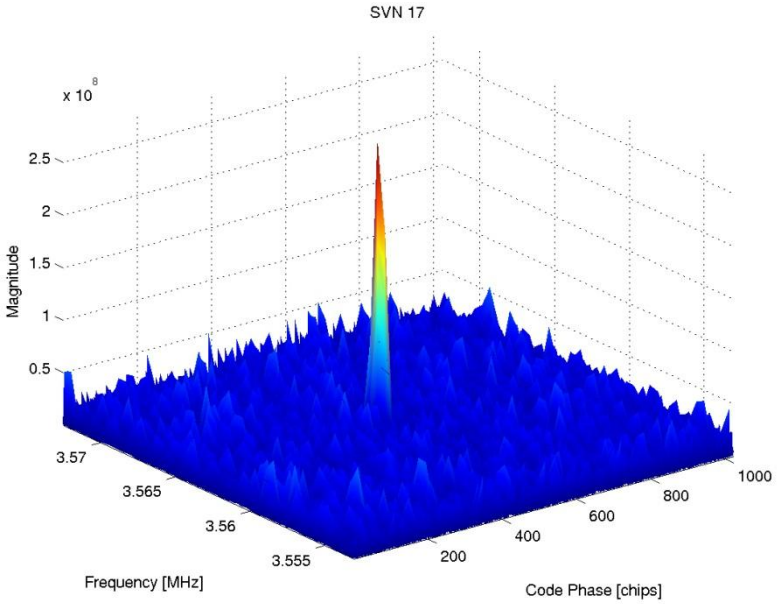

Figure 3.7: An example of acquisition results for a visible satellite [10].

3.6.2 Tracking

While the acquisition identifies the coarse values of frequency and code phase, the tracking aims at refining these values, keeping track of the GPS signals continuously, and decoding the navigation data. The tracking includes both code tracking and carrier frequency tracking. Both of them run continuously to follow the change over time of incoming frequency and code phase. If the tracking is lost for any satellite, the acquisition needs to be re-run for such this satellite.

3.6.2.1 Carrier Tracking

Phase lock loops (PLL) or frequency lock loops (FLL) are often used for tracking the carrier frequency of GPS signal. A simple block diagram of tracking based on PLL is shown in Fig. 3.8.

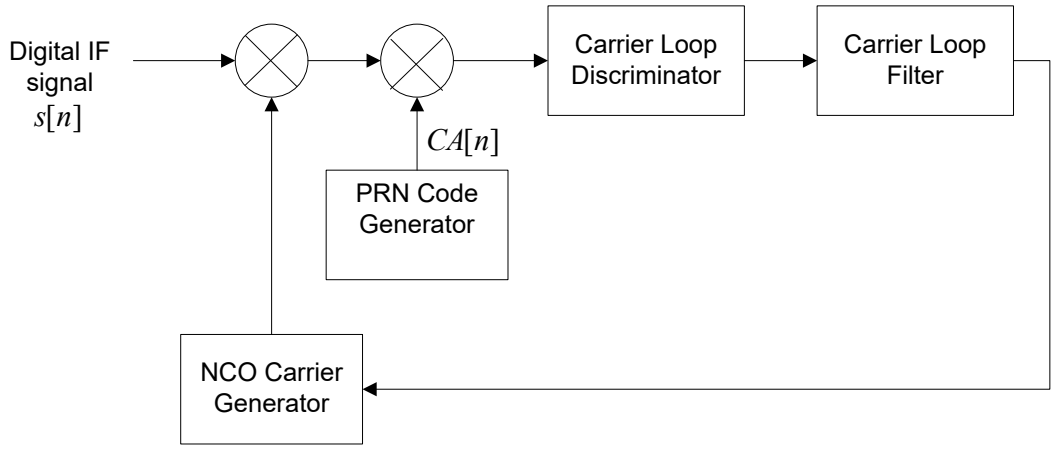

Fig 3.8: The block diagram of tracking based on PLL at GPS receiver.

In general, the input signal is multiplied by a generated carrier wave replica to remove the carrier wave. Then the signal is multiplied by a generated PRN code replica to decode the navigation data. The purpose of carrier loop discriminator block is determining the phase error of the generated carrier wave. The phase error is filtered by carrier loop filter block and then feed-backed to the numerically controlled oscillator (NCO). The NCO carrier generator will adjust the carrier frequency of generated wave to replicate the incoming signal. As we know that the GPS signal is bi-phase modulated. Hence, the simple PLL which is sensitive to $180°$ phase shifts can cause the error on navigation data decoding. Therefore, the Costas loop, a modified of PLL, can deal with this issue. The block diagram of tracking based on Costas loop is described in Fig. 3.9. The in-phase (I) and quadrature (Q) signals are conducted by multiplying the signal with the generated carrier wave and $90°$ phase shifts of the generated carrier wave, respectively as follows:

$$D^k[n]\cos[\omega_{IF}n]\cos[\omega_{IF}n+\varphi_{carrier}]=\frac{1}{2}D^k[n]\cos[\varphi]+\frac{1}{2}D^k[n]\cos[2\omega_{IF}n+\varphi]\ , \quad (3.15)$$

$$D^k[n]\cos[\omega_{IF}n]\sin[\omega_{IF}n+\varphi_{carrier}]=\frac{1}{2}D^k[n]\sin[\varphi]+\frac{1}{2}D^k[n]\sin[2\omega_{IF}n+\varphi]\ , \quad (3.16)$$

where φ is the phase difference between the carrier phase of the received GPS signal and the generated carrier phase from the receiver. The final I and Q signal are obtained after low-pass filtering as:

$$\begin{aligned} I^k &= \frac{1}{2} D^k[n]\cos[\varphi_{carrier}], \\ Q^k &= \frac{1}{2} D^k[n]\sin[\varphi_{carrier}]. \end{aligned} \tag{3.17}$$

Hence, the phase difference φ can be computed from (3.17) as:

$$\begin{aligned} \frac{Q^k}{I^k} &= \frac{\frac{1}{2} D^k[n]\sin[\varphi]}{\frac{1}{2} D^k[n]\cos[\varphi]} = \tan[\varphi_{carrier}], \\ \varphi_{carrier} &= \arctan\left(\frac{Q^k}{I^k}\right). \end{aligned} \tag{3.18}$$

The phase difference $\varphi_{carrier}$ is considered the output of the discriminator which feedback to the NCO carrier generator.

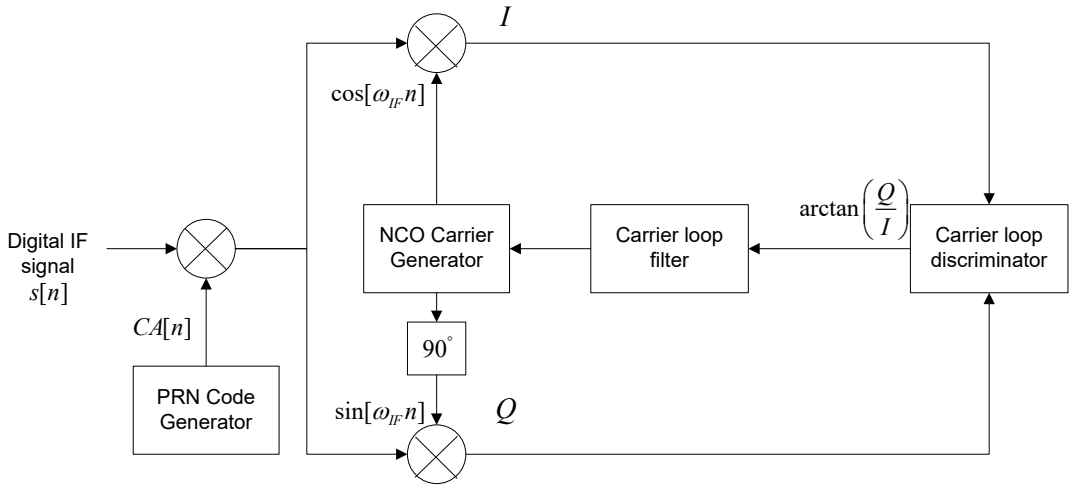

Figure 3.9: The block diagram of tracking based on Costas loop at GPS receiver.

3.6.2.2 Code Tracking:

Delay Lock Loop (DLL) is used for tracking the code of GPS signal. The concept of DLL is to correlate the incoming signal with three replicas of the code including early code, prompt code, and late code. The prompt code is generated according to the code phase of the

incoming signal. While the early code and late code are generated by shifting the prompt code by a haft of chip to the left and right, respectively. An example of the correlations between incoming code and three code replicas are illustrated in Fig 3.10.The prompt code has the highest correlation while the early code and late code have similar correlation. Hence, the code tracking loop perfectly aligns the replica of the incoming code. On the other hand, if the late code has the highest correlation, the code phase must be decreased. Similarly, if the early code has the highest correlation, the code phase must be increased.

The code discriminator factor, φ_{code}, is based on the ratio of the early and late code as:

$$\varphi_{code} = \frac{Early}{Late} . \tag{3.19}$$

The generated code is perfectly aligned the code of incoming GPS signal if φ_{code} equals to 1. If the φ_{code} greater than 1, the PRN code generator will shift the code to the right. Inversely, if the φ_{code} is smaller than 1, the PRN code generator will shift the code to the left.

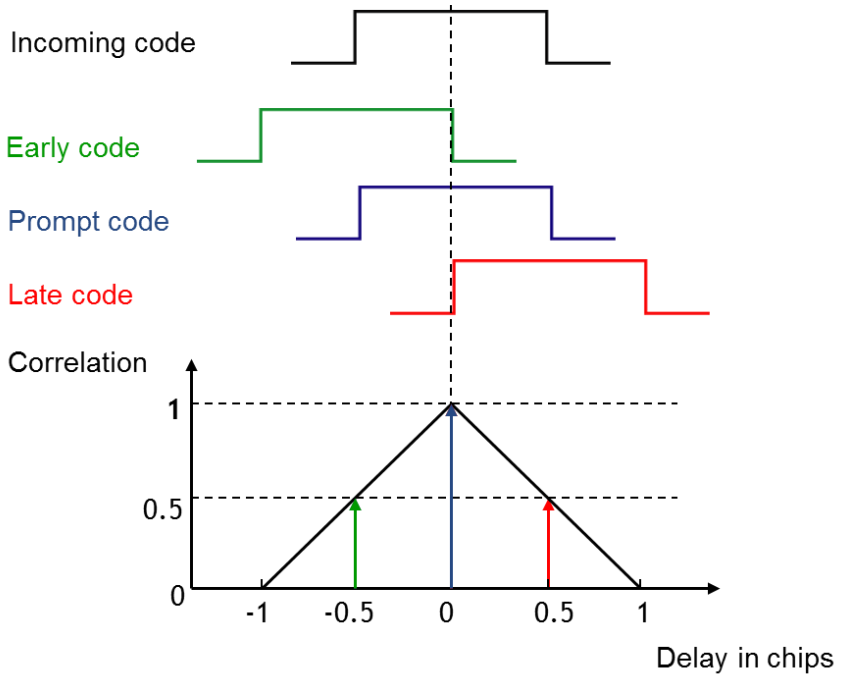

Figure 3.10: The correlations between incoming code and three code replicas.

A block diagram of code tracking based on DLL for in-phase (I) signal is shown in Fig 3.11. The I signal is multiplied with three code replicas mentioned above to obtain the early I (I_E), prompt I (I_P), and late I (I_L). The I_E, I_P, and I_L are compared to each other to

determine which one has the highest correlation. Then, the code phase is adjusted to enhance the accuracy of code tracking.

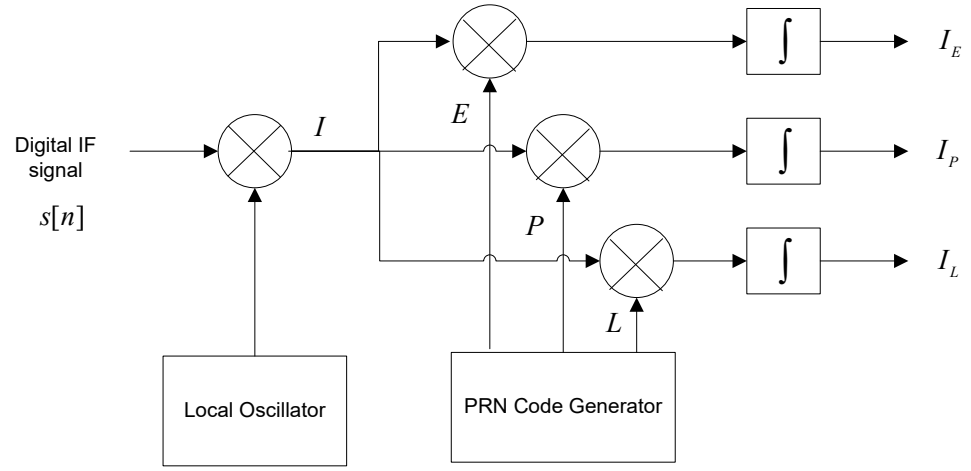

Figure 3.11: The block diagram of code tracking based on DLL for in-phase (I) signal.

Finally, the complete block diagram of tracking including code tracking and carrier tracking are shown in Fig. 3.12.

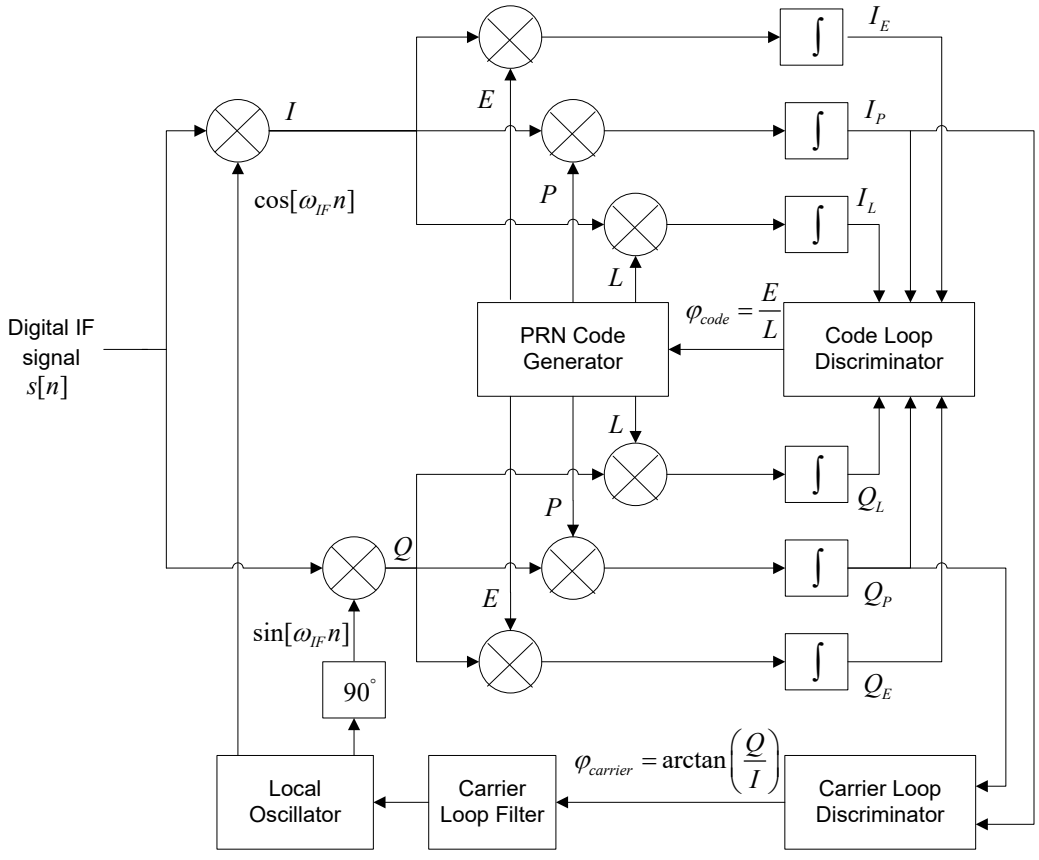

Figure 3.12: The complete block diagram of tracking at GPS receiver.

Chapter 4

Ionospheric Scintillation Monitoring using software GPS receiver at Chumphon station, Thailand

4.1 Introduction

The ionospheric irregularities caused by sporadic solar disturbances dramatically impact the satellite communication. Particularly, the satellite signals propagating through the ionosphere are irregularly fluctuated in terms of signal amplitude and carrier phase, known as a scintillation phenomenon. The scintillation may result in degraded performance of the tracking loop in the receiver. In the worst case, strong scintillation is a potential cause of loss-of-lock and even loss of satellite signal. Therefore, monitoring the scintillation is essential for ionospheric study as well as attempting to improve satellite signal more precisely and continuously [14].

The ionospheric scintillation is characterized by phase scintillation and amplitude scintillation. The phase scintillation is observed from the standard deviation of detrended carrier phase $\sigma_{\Delta\phi}$ while the S4 index describes the severity of the amplitude scintillation. Historically, scintillation monitoring based on single L1 frequency GPS receiver has been widely used due to its low cost, mobility and also good performance. The single L1 frequency receiver is able to filter the low frequency systematic effects out such as satellite motion, clocks, selective availability, and the troposphere [15].

We use the GPS/GALILEO L1 RF Recorder of iP-Solutions to receive the RF signal of GPS satellites on L1 frequency (1575.42 MHz) and pre-process the data on the computer. Then, the S4 index can be computed following the process of S4 detrending and ambient-noise removal. In this chapter, we present the results of S4 index at Chumphon station, Thailand (geographic latitude 10.72°N, longitude 99.37°E, and magnetic latitude 3.3°N) during 85 minutes from 19:55 to 21:20 Local Time (LT) on March 29, 2012 since there is a plasma bubble occurrence on that day.

In Section 4.2, the methodology of S4 index computation is described. Then, the results are presented and discussed in Section 4.3. Finally, the summary is given in Section 4.4.

4.2 Methodology

The software GPS receiver system contains a choke-ring antenna, a GPS L1 RF recorder, and a pre-processing software installed in a computer as shown in Fig. 4.1. Firstly, the L1 RF recorder receives the RF signal of GPS satellites on L1 frequency with a sampling rate of 16 MHz, down-converts the RF signal to the immediate frequency (IF) signal with a frequency of 4.12 MHz, and records on computer as digitized intermediate frequency (DIF) data. The interval time for each DIF file is 17 minutes.

Figure 4.1: The software GPS receiver system.

Afterwards, the DIF data are processed by using Borre's open source MATLAB receiver with respect to the acquisition, tracking, and navigation data decoding [16]. The acquisition step identifies the visible GPS satellites to the receiver. As a result, the frequency and code phase of the GPS signal of each visible satellite is determined. While the tracking step which includes code tracking and carrier frequency tracking keeps track of the GPS signal continuously. The in-phase (I) and quadrature (Q) signals are generated by multiplying the digitized IF signal with sine and cosine components. Then, the early, prompt, and late code generators are multiplied by I and Q and integrated to conduct the output of channel correlators. The brief block diagram of tracking process which focuses on the prompt code of I and Q signal is described in Fig. 4.2.

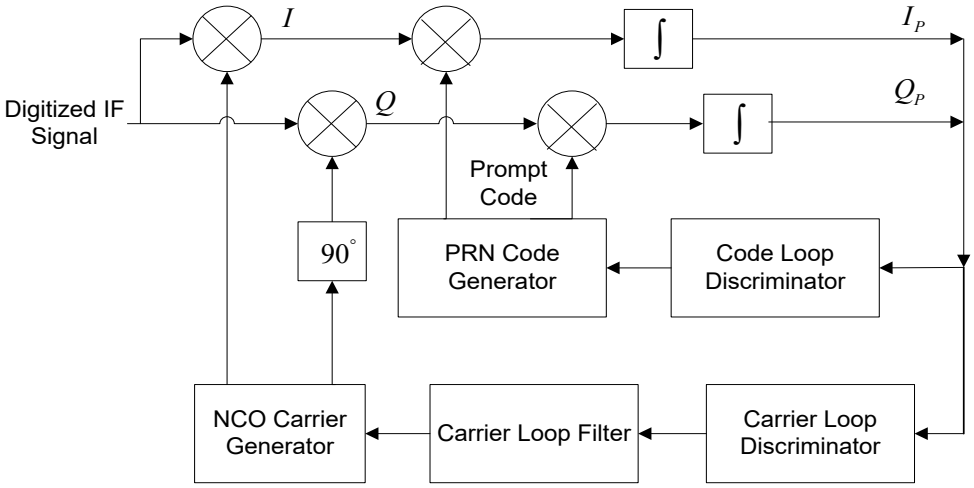

Figure 4.2: The block diagram of a tracking channel on the GPS receiver.

4.2.1 $S4$ Computation

The total $S4$ index which is basically derived from the intensity of received signal can be computed from the prompt I (I_P) and Q (Q_P) correlator outputs. In details, the raw signal intensity (SI) is proportional to the difference between the narrow-band power (NBP) and wide-band power (WBP) which are computed at every 20 milliseconds from [15]:

$$\begin{aligned} NBP &= \left(\sum_{i=1}^{20} I_i\right)^2 + \left(\sum_{i=1}^{20} Q_i\right)^2, \\ WBP &= \sum_{i=1}^{20} \left(I_i^2 + Q_i^2\right). \end{aligned} \tag{4.1}$$

where I_i and Q_i are the i^{th} samples of I and Q sequences.

The total $S4$ index can be computed by

$$S4_T = \sqrt{\frac{E\left(SI^2\right) - E^2\left(SI\right)}{E^2\left(SI\right)}}. \tag{4.2}$$

However, the $S4$ computation needs to deal with two issues including $S4$ detrending and ambient noise removal. The raw signal intensity is detrended by using a 6^{th}-order low-pass Butterworth filter with a 0.1 Hz cutoff frequency [15]. Then, the final signal intensity is

conducted by dividing the input of the low-pass filter, $\left(NBP–WBP\right)_k$, by the output of the low-pass filter, $\left(NBP–WBP\right)_{lpf,k}$, as

$$SI_k = \frac{\left(NBP–WBP\right)_k}{\left(NBP–WBP\right)_{lpf,k}}. \tag{4.3}$$

In addition, the $S4$ due to ambient noise is [15]

$$S4_{N_0} = \sqrt{\frac{100}{C/N_0}\left(1+\frac{500}{19C/N_0}\right)}, \tag{4.4}$$

where C/N_0 is the carrier-to-noise density.

Finally, the $S4$ index is obtained after removing the effects of the ambient noise from the total $S4$ index, given as

$$S4 = \sqrt{\frac{E\left(SI^2\right)-E^2\left(SI\right)}{E^2\left(SI\right)}-\frac{100}{C/N_0}\left(1+\frac{500}{19C/N_0}\right)}. \tag{4.5}$$

4.2.2 C/N$_0$ Estimation

For the carrier-to-noise density estimation, there are various algorithms with low complexity such as Beaulieu's method, signal-to-noise variance method, moment method, real signal-complex noise method, narrowband-wideband power ratio method, and others. Among them, the signal-to-noise variance (SNV) is appropriate for medium-to-low *SNRs* (C/N_0 range from 30 to 55 dB-Hz) while the moment method is appropriate for high *SNRs* (C/N_0 above 55 dB-Hz) [17]. Since the C/N_0 is typically measured in a range of 35to 50dB-Hz for the GPS L1 RF recorder, we select the SNV as C/N_0 estimation algorithm in this work.

The output signal of channel correlators, $r_c[n]$ can be also written as

$$r_c[n] = \sqrt{P_d}D[n] + \sqrt{P_n}\eta[n], \tag{4.6}$$

where $D[n]$ and $\eta[n]$ are the navigation bit and noise samples, respectively, while P_d and P_n are data and noise power, respectively. The estimated total power, P_{tot}, is basically a sum of P_d and P_n. According to SNV method, the total and data power can be computed by

$$P_{tot} = \frac{1}{20}\sum_{i=1}^{20}\left(I_i^2+Q_i^2\right), \qquad P_d = \left(\frac{1}{20}\sum_{i=1}^{20} I_i\right)^2. \tag{4.7}$$

The signal-to-noise density at the output of channel correlators, λ_c, is the ratio of data power to noise power as

$$\lambda_c = \frac{P_d}{P_{tot}-P_d}. \tag{4.8}$$

The C/N_0 estimation from the SNV method is defined as

$$\frac{C}{N_0} = \lambda_c B_{eqn} = \frac{1}{T_{int}} \cdot \frac{\left(\sum_{i=1}^{20} I_i\right)^2}{20\sum_{i=1}^{20}\left(I_i^2+Q_i^2\right)-\left(\sum_{i=1}^{20} I_i\right)^2}, \tag{4.9}$$

where B_{eqn} is the normalized equivalent noise bandwith and equal to the inversion of intergation time, T_{int} [17].

4.3 Results and Discussions

The 85-minute GPS data used for the experiment has been recorded at Chumphon station from 19:55 to 21:20 LT on March 29, 2012. There are 6 visible GPS satellites during that observational period including PRN03, PRN07, PRN11, PRN13, PRN19, and PRN23.

We computed the S4 index of PRN03 following the procedures mentioned in Section 4.2. The GPS data of PRN03 are availabe during the first 34 minutes of the observational time. The amplitude of the I-channel of PRN03 is plotted in Fig. 4.3. There is a high fluctuation of the I-channel amplitudes starting from the 20th-minute to the end due to the scintillation. Figure 4.4 illustrates the zoomed in I-channel amplitude during scintillation occurrence. The intensity of the raw signal and detrended signal are presented in Fig. 4.5. As we can see, the results fluctuate during scintillation, but the low-pass filter is able to capture the trend of the signal intensity. The detrending process has been done by normalizing the signal intensity as shown in Fig. 4.6. Afterwards, the carrier-to-noise density is estimated by applying the SNV method as shown in Fig. 4.7. Finally, the total S4 (*S4-total*) and the ambient-noise-corrected S4 (*S4-corr*) are plotted

in Fig. 4.8. Furthermore, the elevation angle of PRN03, shown in Fig. 4.9, declines from about 50 to 30. We note that the elevation angle of PRN03 is under 40 during the fluctuation of S4 index.

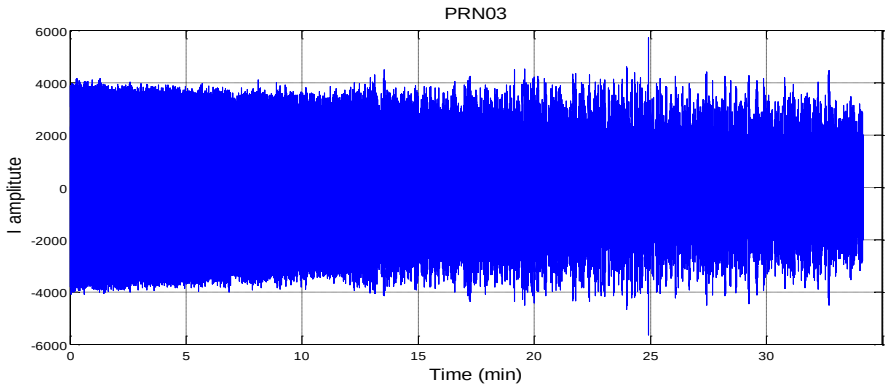

Figure 4.3: I-channel amplitude of PRN03 during 34 minutes on March 29, 2012.

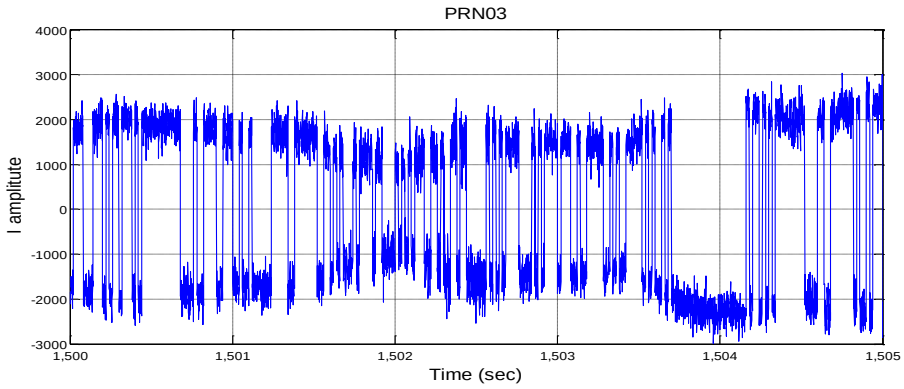

Figure 4.4: The variation of I-channel amplitude of PRN03 due to scintillation.

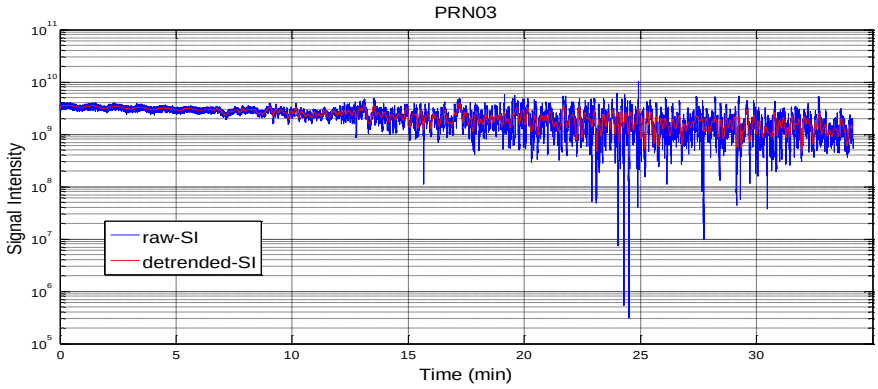

Figure 4.5: The intensity of the raw signal and detrended signal of PRN03.

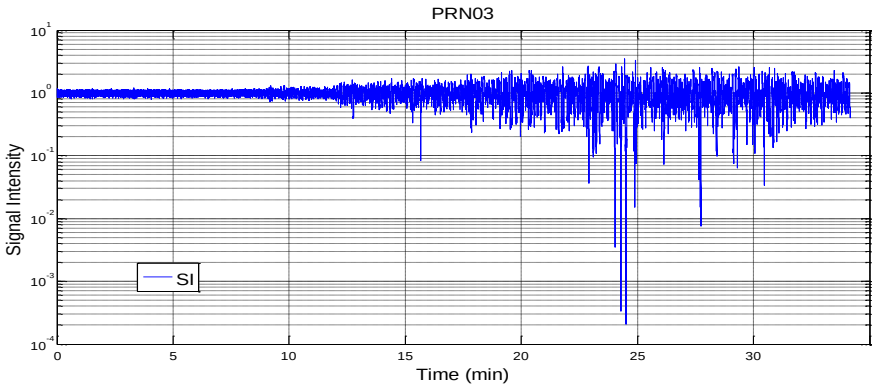

Figure 4.6: The signal intensity of PRN03.

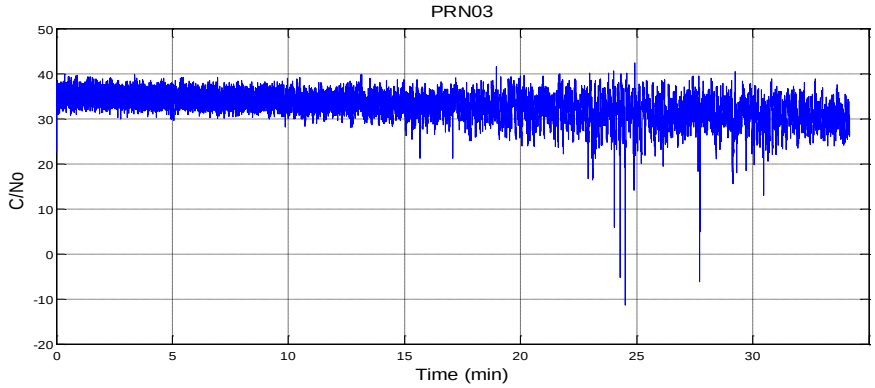

Figure 4.7: The C/N_0 result of PRN03.

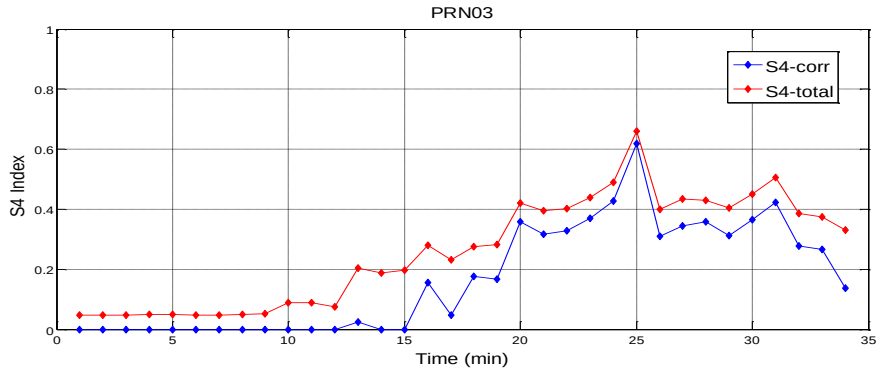

Figure 4.8: The total $S4$ index and ambient-noise-corrected $S4$ index of PRN03.

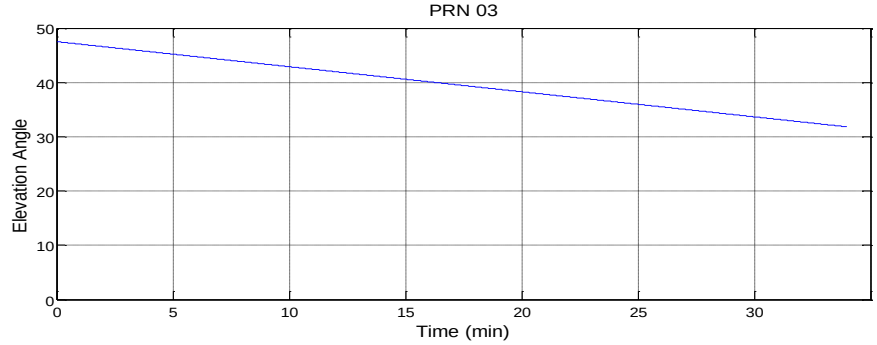

Figure 4.9: The elevation angle of PRN03.

In addition, the elevation angle and the computed S4 index for the other visible GPS satellites are shown in Fig. 4.10. The results show the strong scintillation in PRN07 during 17-minute available data, while no scintillation occurs for PRN11, PRN13, PRN19, and PRN23. The elevation angle of PRN07 is under 40, whereas the other visible GPS satellites have a high elevation angle. In details, the trajectory of all visible GPS satellite is plotted in Fig. 4.11. The PRN03 and PRN07 locate near the horizon so that their elevation angle is low. This may be a reason of high fluctuation of the S4 index.

Figure 4.12 shows the S4 indices of all visible GPS satellites for the entire data. The color line represents the S4 index variation from 0 (blue) to 1 (red). The ionosphere irregularities such as plasma bubble are considered as the cause of high S4 index in PRN03 and PRN07. When the plasma bubble occurs, the electron density around this area depletes leading to the high variation of total electron content (TEC). Thus, it affects the GPS signal propagating along the satellite-receiver path and results in the scintillation.

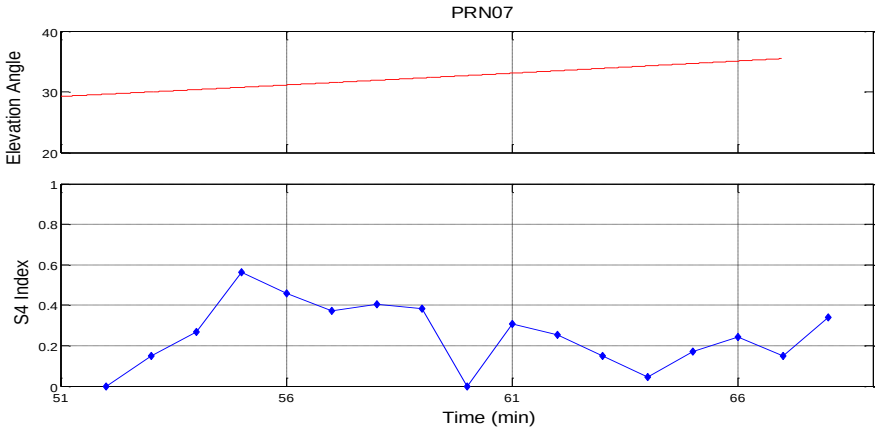

(a)

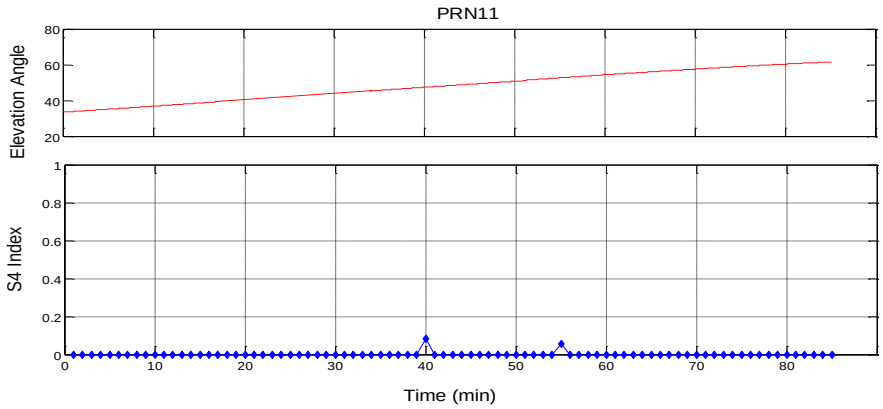

(b)

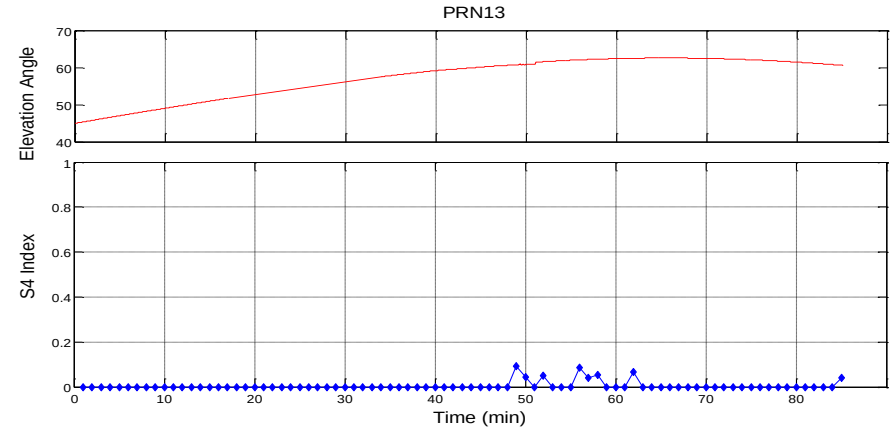

(c)

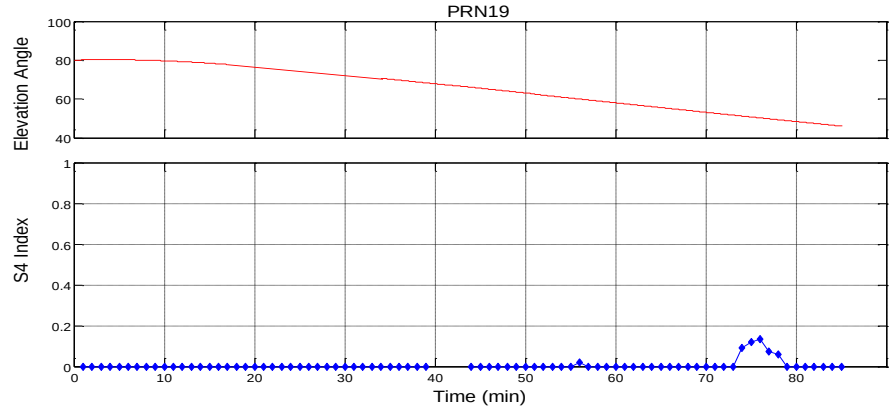

(d)

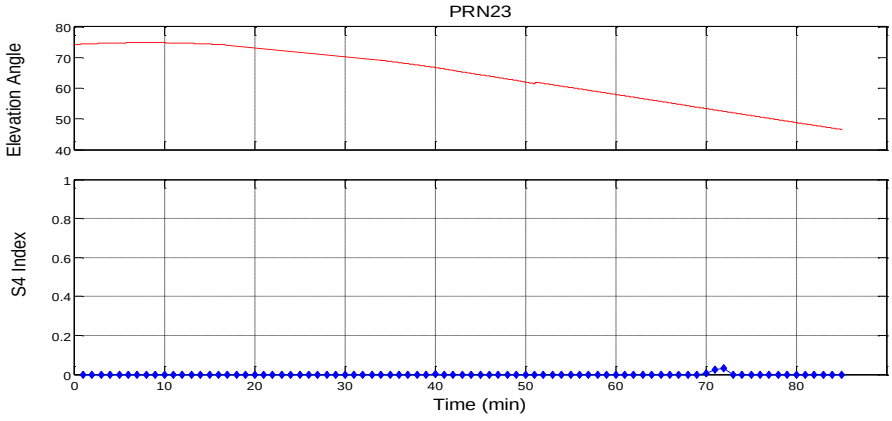

(e)

Figure 4.10: The elevation angle and the ambient-noise-corrected S4 index of PRN07 (a), PRN11 (b), PRN13 (c), PRN19 (d), and PRN23 (e).

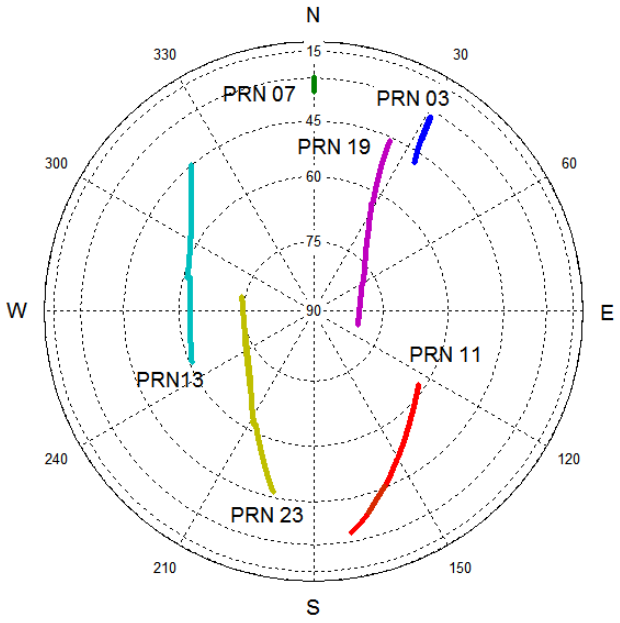

Figure 4.11: Sky plot of the trajectory of all visible GPS satellites.

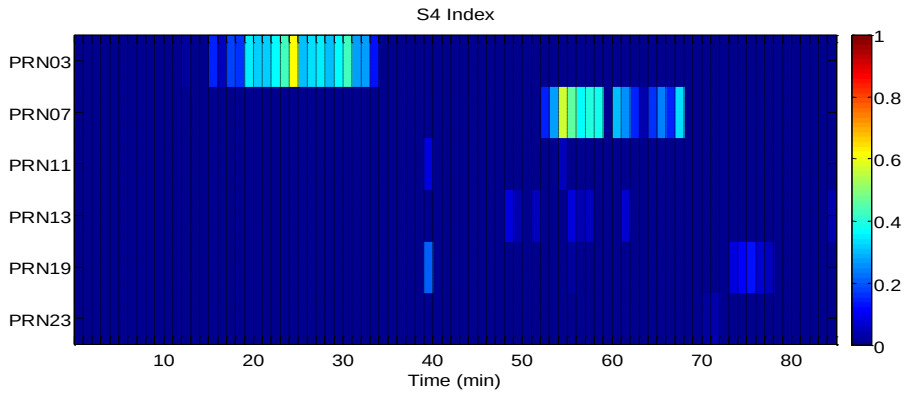

Figure 4.12: The S4 index for all visible GPS satellites.

4.4 Summary

Ionospheric scintillation monitoring is important to the ionospheric study and improving the precision and continuity of GPS signal. In this work, we derived the S4 index from the raw GPS data of a GPS L1 RF recorder. The final S4 index is achieved after detrending and ambient noise removal. For C/N_0 estimation, the SNV method is applied. The scintillation occurrence in some satellites during the observational time agrees with the plasma bubble occurrence on that day.

Chapter 5

Loss-of-Lock Statistics from the GPS receiver near Suvarnabhumi airport, Thailand

5.1 Introduction

The irregularities of the ionosphere can cause the scintillations phenomena on trans-ionospheric signals. At GPS receiver, it results in attenuation/ reinforcement of signal intensity, phase noise, and cycle slips. The loss of phase lock, or loss-of-lock (LOL) occurs when the phase fluctuates too rapid for the receiver to track the signal. Moreover, the loss-of-lock on carrier phase may lead to loss of signal. In that case, the communications between the GPS satellites and the GPS receiver are disrupted until the receiver is able to track the signal again. The availability of GPS signals is significant in many fields related to human life including aeronautical application. The navigation of aircraft based on only GPS is inadequate to meet the high safety requirement. Therefore, the ground-based augmentation system (GBAS) [18] and satellite-based augmentation system (SBAS) have been applied to improve the availability, precision, and reliability of the navigation signal [19]. However, both GBAS and SBAS systems are also affected by the ionospheric irregularities which potentially cause the loss-of lock and loss-of-signal. Hence, studying the LOL statistics around the airport area is important.

In this research, the GPS data have been collected and analyzed during 2010 at KMITL station. The location is close to the Suvarnabhumi international airport, Thailand. The data are converted into the Receiver Independent EXchange Format (RINEX) containing the GPS measurements. Then, we derived the number of visible GPS satellites with loss-of lock, the probability of visible GPS satellites with loss-of lock, and the number of usable GPS satellites. From these results, the ionospheric effects on both GPS frequency carriers are compared. We find that the loss-of lock occurrence is related to the rate of TEC change index (ROTI). Furthermore, the correlation between the elevation angles and the number of visible GPS satellites with loss-of lock is studied. The results demonstrate that the number of visible GPS satellites with loss-of lock decreases as the elevation angles increase.

In Section 5.2, the methodology of determining the loss-of lock statistics is proposed. The experimental results are then presented and discussed in section 5.3. Finally, the summary is made in section 5.4.

5.2 Methodology

The KMITL GPS station (13.73˚N, 100.78˚E), located five kilometers away from the Suvarnabhumi international airport, is a part of South-East Asia Low Latitude Ionospheric Network (SEALION) project. We use the TOPCON Legacy_E GPS receiver, with choke-ring antenna, as shown in Fig. 5.1, to obtain the RINEX files with the C_1, P_1, P_2, L_1 and L_2 parameters at every 10-second interval.

Choke – ring Antenna *Dual – Freq GPS Reciever* *PC*

Figure 5.1: The KMITL GPS station system.

5.2.1 RINEX file definition

The Receiver Independent EXchange Format (RINEX), developed by the Astronomical Institute of the University of Berne, first time appeared in 1989 [20]. It is a standard data format obtained from the raw GPS data and easily exchanges between different computer systems. The RINEX has been modified to adapt to new satellite communication system and new type of measurements. The RINEX version 2.10, used for this work, is capable of measuring pseudoranges, carrier-phases and Doppler systems for not only Global Positioning System (GPS) but also Global Navigation Satellite System (GLONASS), European Geostationary Navigation Overlay Service (EGNOS), and Wide Area Augmentation System (WAAS).

There are three types of RINEX files: Observation file, Navigation file, and Meteorological data file. In our research, only the Observation file (O-file) of RINEX 2.1 is explored for LOL investigation. The collected GPS measurements include pseudorange using C/A code on L_1 frequency (C_1), pseudorange using P-code on L_1 frequency (P_1), phase

measurements on L_1 frequency (L_1), doppler frequency on L_1 frequency (D_1), pseudorange using P-code on L_2 frequency (P_2), phase measurements on L_2 frequency (L_2), and Doppler frequency on L_2 frequency (D_2).

5.2.2 Loss-of-Lock Indicator

We extract the Observation RINEX file from KMITL GPS station for PRN3 at 0.00 am on October 2nd, 2010 (UTC) as shown in Fig. 5.2. The observation data contain the value of parameters C_1, P_1, P_2, L_1, and L_2 followed by two numbers at the end. The first number is Loss-of-Lock Indicator (LLI), which is the fourth digit after the decimal point of the data. In the figure above, the LLI does not exist on C_1 and L_1 data while the LLI equals to 4 on P_1, P_2, and L_2 data. In addition, the LLI, which ranges from 0 to 7, can be translated into three binary bits. The value of each binary bit indicates one of the following LOL statistics [21], i.e,

a) 0 or Blank: Ok or not known,
b) Bit 0 sets to 1: Loss-of-lock between previous and current observation (cycle slip possible),
c) Bit 1 sets to 1: Opposite wavelength factor to the one defined for the satellite by the previous wavelength fact L1/2 line. Valid for the current epoch only, and
d) Bit 2 sets to 1: Observation under Anti-spoofing (may suffer from increased noise) ,

where bits 0 and 1 for phase only.

As we can see, when the bit 0 is set to 1, or a cycle slip occurs, then it means the loss-of lock occurs. For example, the value of LLI is 1 from the binary sequence '001', and then it means there is a cycle slip. In another case, if the LLI is 4, it will be translated into '100,' therefore an anti-spoofing is present.

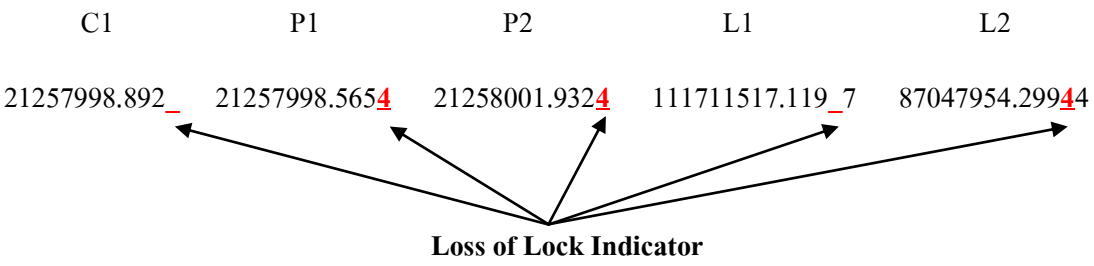

Figure 5.2: An example of observation data.

5.2.3 Probability of Loss-of-Lock

After obtaining the LLI value from data of C_1, P_1, P_2, L_1, L_2, we know whether an observed GPS satellite has loss-of lock or not. The GPS satellite that is seen by a receiver is called the visible satellite. Thus, in each epoch, we can compute the number of visible GPS satellites and the number of visible GPS satellites with LOL corresponding to C_1, P_1, P_2, L_1, and L_2. These are the important parameters to help us investigate the LOL statistics. We can extend the observation period to obtain these results for one month and one year. In order to study the LOL statistics, we define two more parameters including the probability of visible GPS satellites with LOL and the number of usable GPS satellites. The probability of visible GPS satellites with LOL, namely, P_{LOL}, can be computed by

$$P_{LOL} = \frac{N_{S,LOL}}{N_V}, \tag{5.1}$$

where N_V, $N_{S,LOL}$ are the number of visible GPS satellites and the number of visible satellites with LOL, respectively.

During the visible time, the GPS satellite that the station can receive data from is called a usable satellite. The number of usable GPS satellites, namely, N_U, is calculated from

$$N_U = N_V - N_{S,LOL}. \tag{5.2}$$

5.2.4 Flow chart of LOL observation

We observed the LOL statistics based on the Observation RINEX file. Firstly, the header section of RINEX file is read to define which parameters are observed in this file. Then, all epochs are read one by one. In each epoch, we obtain the number of visible GPS satellites and the values of C_1, P_1, P_2, L_1, and L_2 of each visible GPS satellite.

By checking the value of LLI, the LOL occurrences can be determined. If the LLI value is 0, 2, 4, or 6 (its bit 0 is equal to zero), the LOL event will not occur. On the other hand, if the LLI value is 1, 3, 5, or 7, the LOL event will occur. In case of non-existence of LLI value, the LOL event occurs when the observation data do not exist, and the LOL event occurs when the observation data exist.

Moreover, we investigate the effect of the elevation angles on LOL statistics. Firstly, we use National Geodetic Survey (NGS) standard GPS Format SP3 files in order to define the

position of each GPS satellite in each epoch [22]. The elevation angles of these satellites are computed from their positions. Then, the elevation angle condition θ is set so that only the satellites with the elevation angles greater than the threshold will be used. Finally, the results only show the number of visible GPS satellites that satisfy the condition. The flow chart of loss-of-lock observation is plotted in Fig. 5.3.

5.3 Results and Discussions

First at all, we start the LOL observation during October, 2010. We choose to observe this month because October represents an autumnal equinox month. The equinox occurs twice a year when the tilt of the Earth's axis is inclined neither away from nor towards the Sun. One effect of equinoctial periods is the temporary disruption of communications satellites, leading to loss of lock and loss of signal. After that we extend the observation into the entire year of 2010.

Firstly, we discuss the results of probability of LOL of C_1, P_1, P_2, L_1, and L_2 component. During October 2010, the probability of LOL on C_1 and L_1 component is zero, indicating that there is no occurrence of LOL. Comparing with the results in October, the probability of LOL on C_1 and L_1 component for the rest of year 2010, shown in Figs. 5.4-5.5, is almost the same. In 2010, there are a few occurrences of LOL on C_1 and L_1 during the equinox, such as March and September. As a result, it can be inferred that the L_1 frequency is not affected by the LOL.

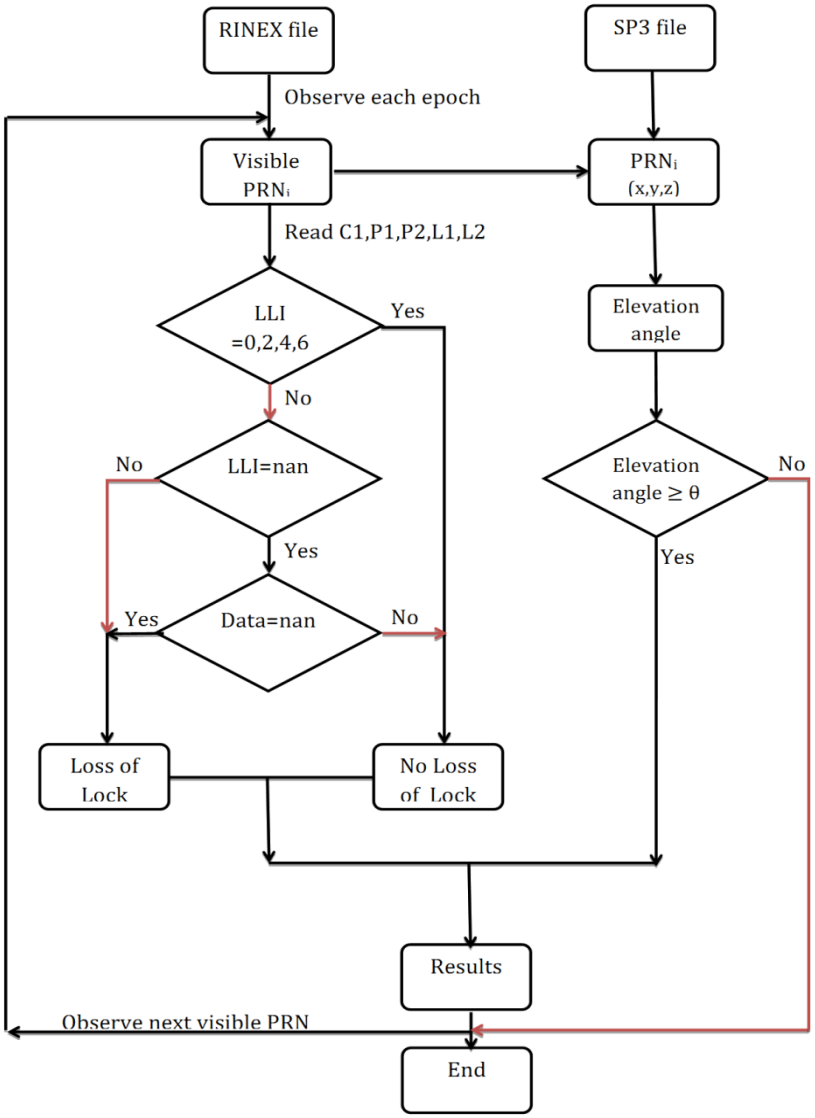

Figure 5.3: Flow chart of loss-of-lock observation.

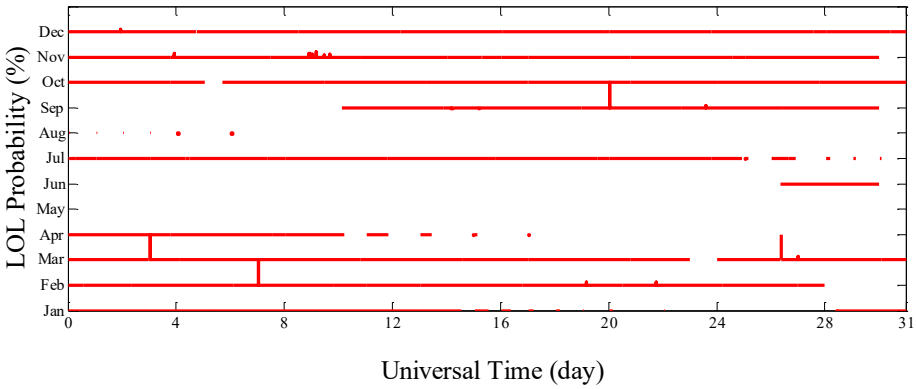

Figure 5.4: Probability of visible satellites with LOL of C_1 in 2010.

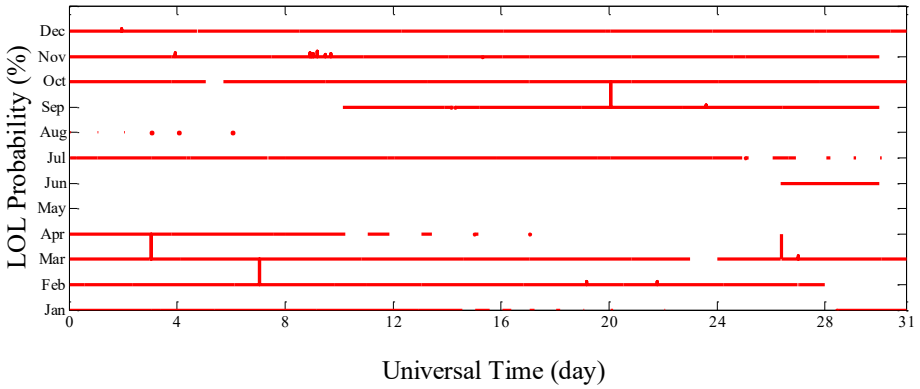

Figure 5.5: Probability of visible satellites with LOL of L_1 in 2010.

On the other hand, we observe the probability of LOL on P_1, P_2, and L_2 component in October 2010. In Figs. 5.6-5.8, the probability of LOL on P_1, P_2, and L_2 varies from 0 to about 0.4. When we observe the data during 2010, we obtain the results which fluctuate from 0 to about 0.4. Compared with the probability of C_1 and L_1, it can be evident that the L_2 frequency is more susceptible to the LOL events than the L_1 frequency.

In addition, in Fig. 5.7, the probability of LOL on L_2 equals 1 during some epochs on 15th, 19th, and 31st. It means all visible satellites have LOL of L_2. Compared with the high fluctuation of ROTI on 15th, 19th October, 2010, shown in Fig. 5.9, it seems that LOL occurrence is related to the ROTI. In general, we collect the epochs that all visible GPS satellites have LOL during 2010. Then, we look at the corresponding ROTI graph on these days as well. As a result shown in Table 5.1, we realized some days in the equinox month with LOL occurring on all the visible satellites, and, in addition, at the same time, the ROTI exhibits high fluctuation.

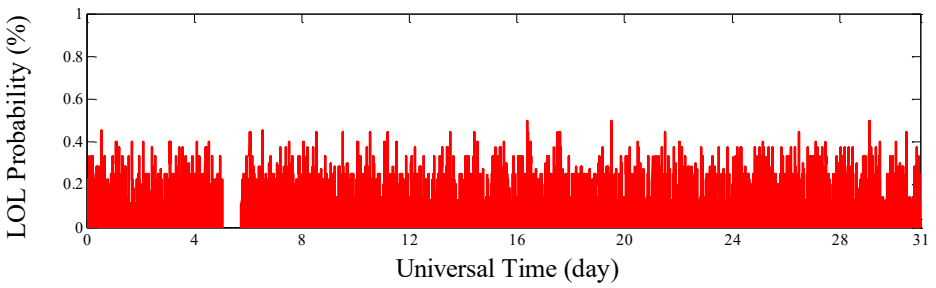

Figure 5.6: Probability of visible satellites with LOL of P_1 in October,2010.

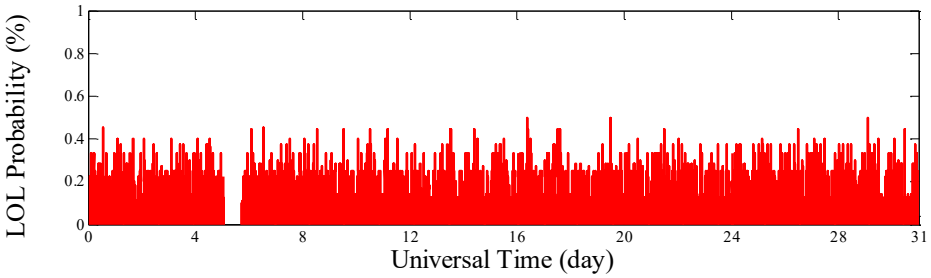

Figure 5.7: Probability of visible satellites with LOL of P_2 in October,2010.

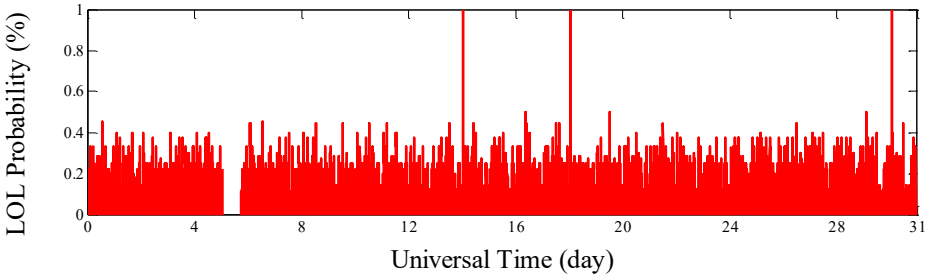

Figure 5.8: Probability of visible satellites with LOL of L_2 in October,2010.

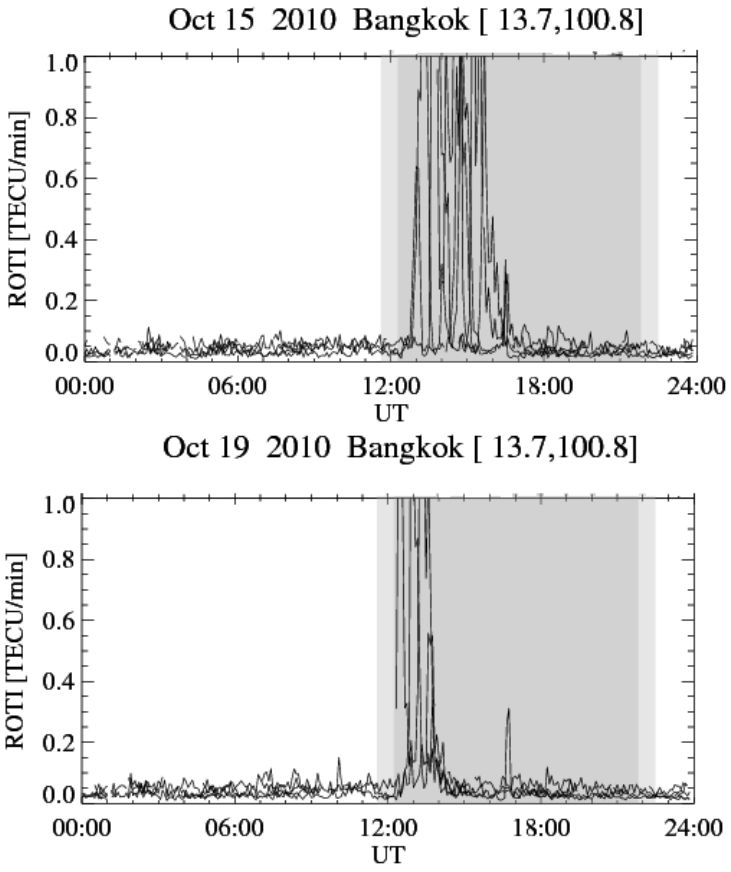

Figure 5.9: High fluctuation of ROTI on 15th, 19th October, 2010 [23].

Table 5.1: The dates with both LOL occurrence and high fluctuation of ROTI

Month	**Days**
March	4^{th}, 21^{st}, 27^{th}, 31^{st}
September	15^{th},17^{th}, 21^{st}
October	15^{th}, 19^{th}

In short, from probability of LOL we find out how susceptible of L_1 and L_2 frequencies from LOL and the relation between LOL events and ROTI. Secondly, we found the number of visible GPS satellites with LOL. Usually, a GPS satellite is visible for about 6 to 7 hours a day when it moves over the receiver station. During the visible time, the GPS station can receive data from the visible GPS satellite. However, when LOL occurs, the station cannot receive data from the visible GPS satellites.

In October, 2010, there is no GPS satellite with LOL of C_1 and L_1. It means all of visible GPS satellites are usable in terms of C_1 and L_1. It is correct when compared with probability of LOL in terms of C_1 and L_1. On the other hand, in Figs. 5.10-5.12, the number of visible GPS satellites with LOL in P_1, P_2, L_2 fluctuates from 0 to about 4. The highest peaks in these figures mean that the highest number of satellites with LOL is according to high probability of LOL.

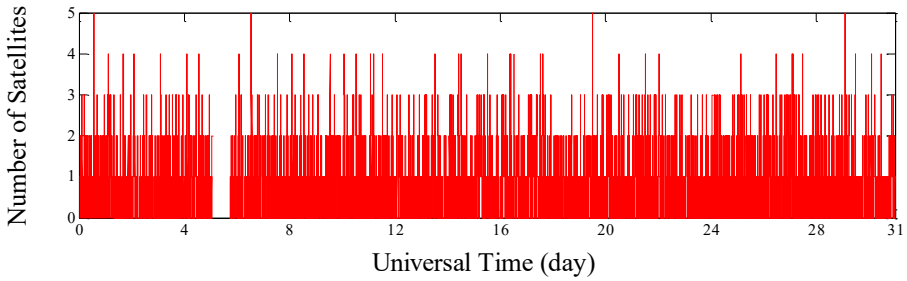

Figure 5.10: Number of visible satellites with LOL of P_1 in October 2010.

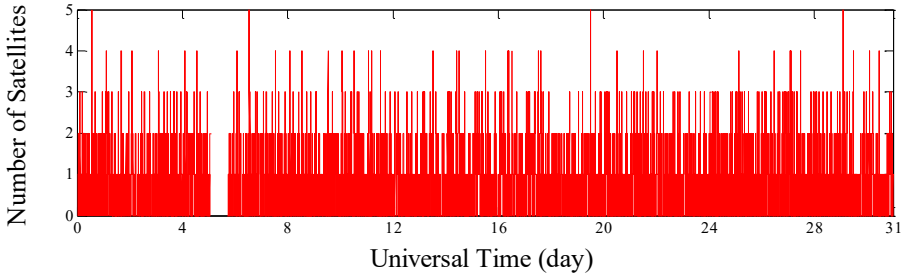

Figure 5.11: Number of visible satellites with LOL of P_2 in October 2010.

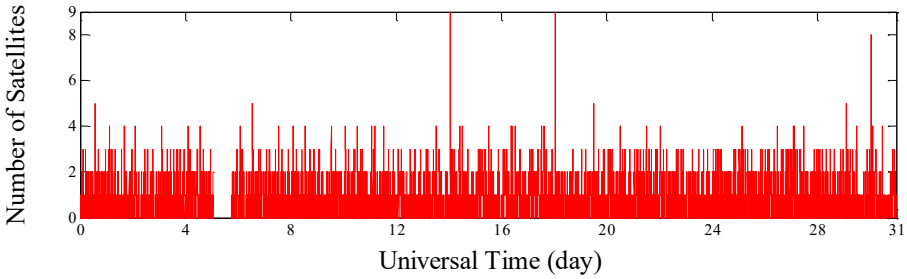

Figure 5.12: Number of visible satellites with LOL of L_2 in October 2010.

In general, we have investigated the number of visible GPS satellites with LOL during 2010. The results show that the number of visible GPS satellites with LOL is less than 5 during almost all of the observed time. It means the LOL event rarely occurs. Therefore, we focus on the epoches that LOL occurs for many GPS satellites. In Figs. 5.13-5.15, we plot the number of visible GPS satellites with LOL of P_1, P_2, L_2 that is greater than 6. While there is no LOL event in C_1 and L_1, the number of LOL events in P_1 is 1. It confirms the stability of L_1 frequency. On the other hand, the number of LOL events in P_2 is 2 and L_2 is 41. Thus, we once again claim that the L_2 frequency is more susceptible to the LOL events that L_1 frequency.

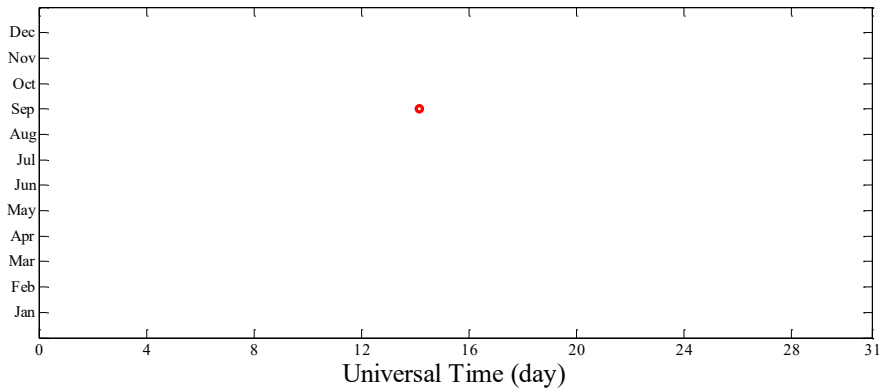

Figure 5.13: Number of visible satellites with LOL of P_1 (greater than 6) in 2010

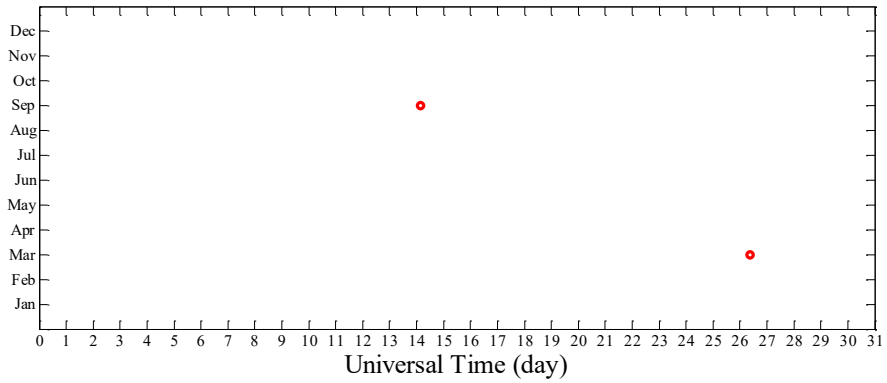

Fig. 5.14: Number of visible satellites with LOL of P_2 (greater than 6) in 2010.

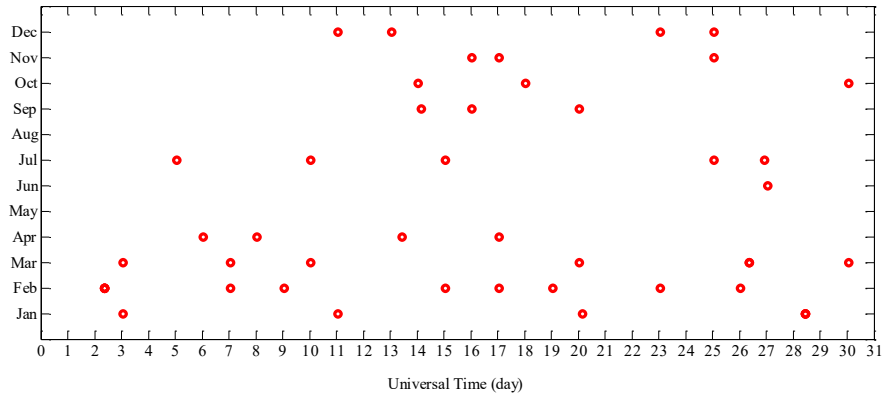

Figure 5.15: Number of visible satellites with LOL of L_2 (greater than 6) in 2010.

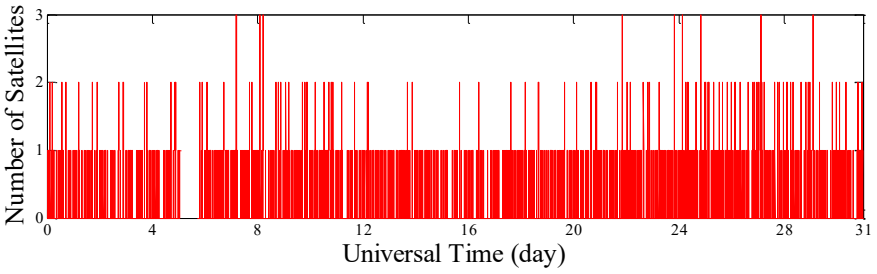

Figure 5.16: Number of visible satellites with LOL of P_1 ($\theta = 30°$) in October 2010.

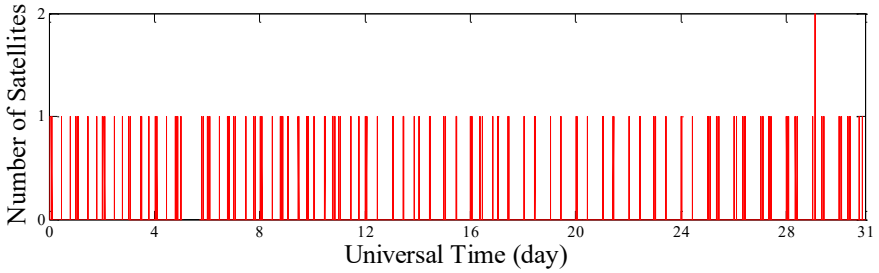

Figure 5.17: Number of visible satellites with LOL of P_1 ($\theta = 40°$) in October 2010.

From the above results, we observe the visible satellites with various elevation angles. However, the LOL can probably occur when the elevation angle is low. Thus, we set up the elevation angle conditions that we only observe the GPS satellites with elevation angles greater than the threshold θ. Finally, we can see how the LOL statistics change when the elevation angles change. In Figs. 5.16-5.17, the maximum number of visible GPS satellites with LOL reduces from 5 to 2 when the elevation angle conditions increase from 0 to 45. The results illustrate that the number of visible GPS satellites with LOL decreases as the elevation angles increase.

5.4 Summary

Loss-of-lock statistics are important for the ionospheric study and the availability of the GPS/GNSS signal. In this work, we observed the GPS data from KMITL station and analyzed the probability of LOL and the number of visible GPS satellites with LOL as well. From the results, it is evident that the L_2 frequency is more susceptible to the LOL events than the L_1 frequency. In addition, the LOL occurrence is related to the high fluctuation of the ROTI and the number of visible GPS satellites with LOL decreases as the elevation angles increase.

Chapter 6

TEC Modeling Based on Improved Neural Network over Chumphon station, Thailand

6.1. Introduction

Ionosphere is an ionized region of the Earth's atmosphere with the periodic and sporadic variation of plasma density. The plasma density, which has periodic diurnal variation, seasonal variation as well as the solar cycle variation, can be predicted using a long period observed data. However, the ionospheric irregularities, which can result in some phenomena such as plasma bubble, are sporadic. Thus, forecasting the plasma density variation under the ionospheric irregularities is definitely a challenge. Total electron content (TEC) is one of the quantities describing adequately such irregularities of the ionosphere. Through the wide temporal and geographical availability of TEC data, several models have been developed to predict the TEC [24], [25], [26], [27]. The well-known one, International Reference Ionosphere (IRI) [25] which is a new empirical standard model, provide accurate prediction in northern hemisphere mid-latitudes. Its data sources are from worldwide ionosonde stations, incoherent scatter radars, the ISIS/ Alouette topside sounders, and in situ measurements on several satellites rockets [28]. However, the IRI model does not predict precisely over the Equatorial Ionization Anomaly (EIA) region such as Thailand because of the significant variation of plasma density in this region and the lack of available observational data.

Artificial neural network has been applied for characterizing the TEC and for future prediction using GPS-derived TEC data [24] or using Faraday-rotation-derived TEC data [29]. With a long period GPS data from dense receiver network [26] predicted the TEC maps with 104 grid points over Europe, while Maruyama [27] developed the two-dimensional TEC maps with 32 grid points over Japan. Recently, there are many efforts for nowcast and forecast TEC over the local region in Brazil [30], South Africa [31], India [32], and Thailand [33].

In this chapter, an improved neural network model is developed from the previous model of Watthanasangmechai [33] which proposed a local TEC modeling based on NN over Thailand. In the previous model, the predicted TEC is compared to the IRI-2007 TEC [34] as

well as the measured TEC. The results show that the previous model is able to predict the TEC well compared to the IRI model. However, the predicted TEC underestimated the measured TEC over all the time of comparison. The error of TEC prediction is probably caused by not only the TEC variation but also the lack of solar activity index such as F10.7 and magnetic activity indices such as Ap and Dst. Hence, the improved model with extended observational period and extended input space of the NN has been developed.

The proposed input space and architecture of the improved NN model are described in Section 6. 2. Afterwards, the performance of the improved model is compared with the previous model in Section 6. 3. Finally, Section 6. 4 provide a summary.

6.2. Neural Network

Artificial Neural Network is an information-processing system which attempts to simulate a simple biological neural network. Inside a human brain, a complex network of over billions of neurons processes the input information and produces the output as human reaction such as thinking, moving, feeling, and so on. The new information will be learned and stored at neurons and connections between them. Similarly, the artificial neural network also contains a number of basic elements called “node,” “neuron,” or “cell.” Its concept is training the network by let the neurons learn new information using a very simple function compared to the biological neural network. The artificial neural network has been applied in many fields such as market forecasting, currency price prediction, speech recognition, telecommunications, space weather forecasting, and others.

6.2.1 Neural Network Architecture

All nodes of the neural network are arranged into three kinds of layers: input layer, hidden layer, and output layer. A simple neural network only contains an input layer and an output layer, so called a single-layer network as shown in Fig. 6.1.a. However, a typical neural network mostly contains an input layer, a single (multiple) hidden layer(s), and an output layer, so called a multilayer network as shown in Fig. 6.1.b. The more hidden layers added to neural network do not improve too much the accuracy of results [35], but in some cases it can make the training easier [36].

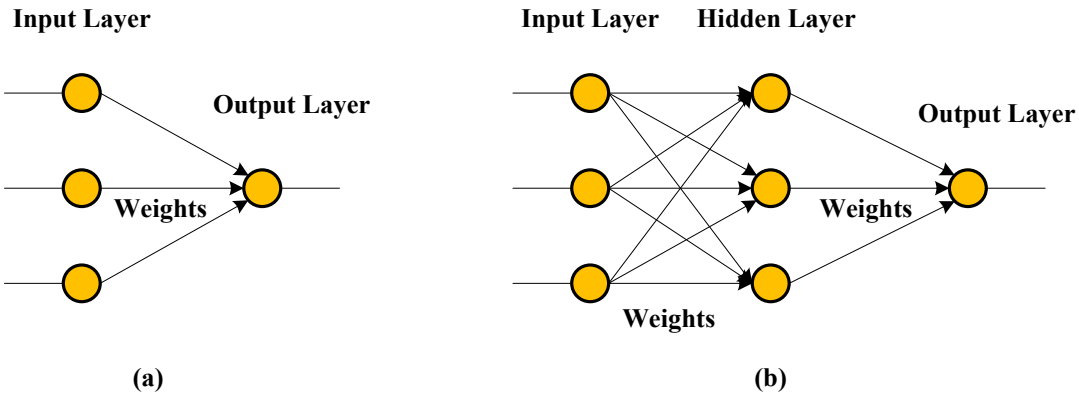

Figure 6.1: The architecture of a single-layer neural network (a) and a multilayer neural network (b).

The NN in which the signal forwarded from input layer to output layer is called a feed-forward NN. At a node, the signal is processed by transfer function. The signal passing a link of two nodes is weighted by associated weight. As a result, the output signal of NN is impacted by all of associated weights inside the model. The output can reach the goal after several routines of adjusting the weights and biases, called training.

6.2.2 Transfer Functions

Transfer functions are applied for a set of inputs of a node to compute the output of such this node. The transfer function can be linear or nonlinear function. All nodes of a layer are probably applied the same transfer function. There are three common transfer functions which are explained below including linear function, binary step function and sigmoid function.

6.2.2.1 Linear Function

The output of a linear transfer function is equal to its input as shown in Fig. 6.2. Its function is defined as follows:

$$f(x) = x \quad for\ all\ x. \tag{6.1}$$

For TEC modeling, the input layer and output layer are often used the linear function.

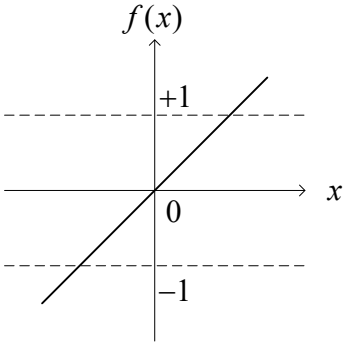

Figure 6.2: Linear Function.

6.2.2.2 Binary Step Function:

The output of a binary step function is a binary (1 or 0) or bipolar (1 or -1) as shown in Fig. 6.3. It sets the output of a neuron to be 0/ -1 if the input is below the threshold, and inversely it sets the output of a neuron to be 1 if the input is over the threshold θ, given as:

$$f(x) = \begin{cases} 1 \ \ if \ x \geq \theta \\ 0 \ \ if \ x \leq \theta . \end{cases} \tag{6.2}$$

The binary step function is often used for classifying the input into two distinct categories.

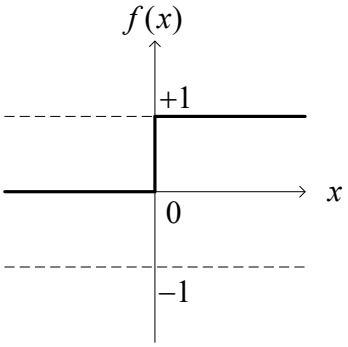

Figure 6.3: Binary Step Function.

6.2.2.3 Sigmoid Function:

There are two common sigmoid functions which are log-sigmoid function and hyperbolic tangent sigmoid function. The output of the log-sigmoid function ranges from 0 to 1 as shown in Fig. 6.4. It is defined as:

$$f(x) = \frac{1}{1+e^{-\sigma x}}\ ,$$
$$f'(x) = \sigma f(x)\left[1 - f(x)\right]\ , \tag{6.3}$$

where σ is the steepness of the log-sigmoid function.

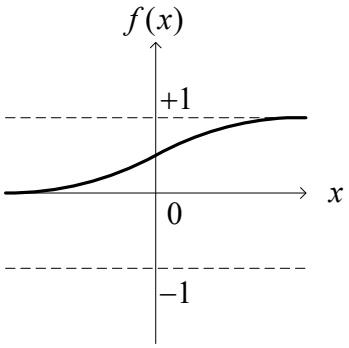

Figure 6.4: Log-sigmoid function.

On the other hand, the output of the hyperbolic tangent sigmoid function ranges from -1 to 1 as Fig. 6.5. It is defined as:

$$h(x) = \frac{e^{x} - e^{-x}}{e^{x} - e^{-x}}\ ,$$
$$h'(x) = [1 + h(x)][1 - h(x)]\ . \tag{6.4}$$

The sigmoid function is commonly used for multi-layer network trained with the backpropagation algorithm.

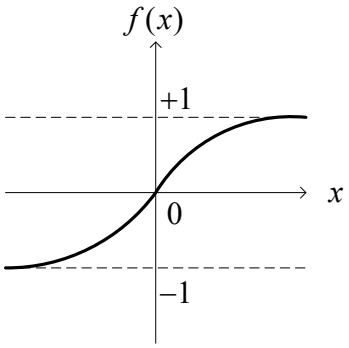

Figure 6.5: Hyperbolic tangent sigmoid function

6.2.3 Backpropagation Algorithm

Historically, backpropagation with a capability of approximating nonlinear data is a common training algorithm [35], [37]. The backpropagation is an approximate steepest descent algorithm for training a multilayer neural network. Generally, its concept is that all associated weights and biases of the neural network are iteratively adjusted to minimize the performance index, known as mean square error (MSE). The backpropagation is a supervised training which means the prior knowledge of input and output set are needed for training. The backpropagation algorithm is described as follows.

The input signal is fed forward, weighted, and then multiplied by the transfer function at each node to finally obtain the output signal. Afterwards, the mean square error (MSE) is computed, and the backpropagation is made to adjust the weight. The MSE is simply calculated by averaging the square of the difference between the target and actual output signal. The MSE is defined as

$$MSE = \frac{1}{N}\sum_{i=1}^{N}(Y_{output,i} - Y_{target,i})^2 , \tag{6.5}$$

where N is the number of data samples, $Y_{output,i}$ and $Y_{target,i}$ are the output signal and the target signal, respectively. Both the MSE and the maximum iteration number are used to stop the training process.

6.3 Proposed Neural Network for TEC modeling:

In this study, the TEC data are collected from January 2005 to December 2010 at Chumphon station, considered an Equatorial latitude station in Thailand, located at Chumphon campus of King Mongkut's Institute of Technology Ladkrabang(geographic latitude 10.72°N, longitude 99.37°E, and magnetic latitude 3.3°N). The period of collected data is a low solar activity period. This study attempts to develop a model which is able to well predict the TEC compared to the previous model. Hence, the artificial neural network with high complexity and nonlinear computation ability is a reasonable model [35].

6.3.1 The operation algorithm of neural network:

The backpropagation has been applied to predict the nonlinear ionospheric parameters with long-term data such as TEC and foF2 [31], [38], [39]. Therefore, we apply a feed-forward

neural network with the backpropagation algorithm for TEC modeling. First at all, the weights and biases within the network are initially set to be small random values. In our model, the input node $X_i\,(i=1:n)$ broadcasts the signal x_i to all hidden-layer nodes $Z_j\,(j=1:p)$.Figure 6.6 illustrates the computation at a specific hidden-layer node Z_j. The input signal x_i is weighted by w_{ij}, and then the input signal z_{in} of the node Z_j is sum of all the weighted input signals and the bias w_{0j} as given by:

$$z_{in} = w_{0j} + \sum_{i=1}^{n} x_i w_{ij} \quad . \tag{6.6}$$

Afterwards, the hyperbolic tangent sigmoid function is applied for hidden-layer to conduct the output signal z_i of the hidden node Z_i as follows:

$$z_j = \tan sig(z_{in\_j}) = \frac{1-e^{-2.z_{in\_j}}}{1+e^{-2.z_{in\_j}}} \, . \tag{6.7}$$

Then, all signals z_i are sent to output nodes $Y_k\,(k=1:m)$. Similarly, the input signal y_{in} of the output node Y_k is given as:

$$y_{in} = w_{0k} + \sum_{j=1}^{m} z_j w_{jk} \quad . \tag{6.8}$$

Finally, the linear function is applied for output layer to obtain the output signal y_k of the output-node Y_k as follows:

$$y_k = purelin(y_{in\_k}) = y_{in\_k} \, . \tag{6.9}$$

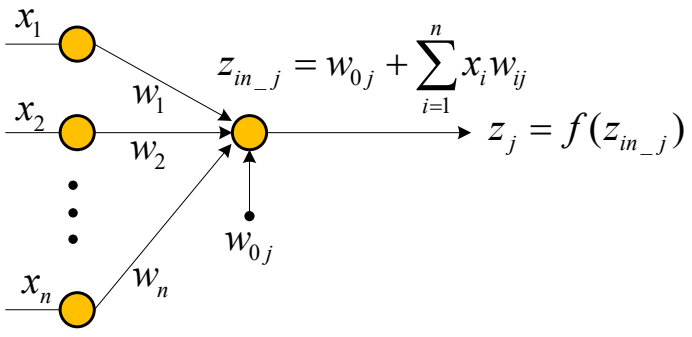

Figure 6.6: Computation at a specific hidden-layer node Z_j.

Among various backpropagation algorithms, the Levenberg-Marquardt is employed because it is the fastest method for training the moderate-sized NN [40]. Our neural network architecture contains an input layer with the impact parameters on the TEC variation, a single

hidden layer, and an output layer with only one node corresponding to the TEC. The number of node in the hidden layer is determined on a trial-and-error basis [39]. The output and target signal of proposed NN are the predicted value of TEC, namely TEC_{pred}, and measured value of TEC, namely TEC_{meas}, respectively. The TEC_{meas} is vertical TEC which is derived from GPS data based on Otsuka's method [41]. The root-mean-square error (RMSE) and normalized root-mean-square error (normalized RMSE), used to evaluate the effective range of proposed NN, are respectively defined as:

$$RMSE = \sqrt{\frac{1}{N}\sum_{i=1}^{N}(TEC_{pred,i} - TEC_{meas,i})^2}, \tag{6.10}$$

and

$$Normalized\ RMSE = \frac{RMSE}{\overline{TEC_{meas}}}, \tag{6.11}$$

where $\overline{TEC_{meas}}$ is averaged value of the TEC_{meas}.

The improved NN is trained with the TEC data of 2005, 2006, 2008, and 2009 and tested with the TEC data of 2007 as same as the previous data. Consequently, the results of the improved NN are compared to the previous NN as well as the measured data. Moreover, the improved NN is tested in 2010 for evaluating its prediction ability.

6.3.2 Input Space

In order to predict the TEC effectively, the input space of the NN must contain various parameters which significantly impact the TEC variation. The factors that affect the TEC variation are categorized into some groups including geographical variation, temporal variation, solar activity and magnetic activity. For geographical variation, the TEC around Thailand considerably varies due to the ionospheric irregularities along this EIA region. For temporal variation, the parameters including hour number (*HR*) and day number (*DN*) are used to reflect the diurnal variation and seasonal variation, respectively. Both parameters are represented by a pair of sine and cosine components to produce the normalized and continuous data [31], [33], [42], [43] as:

$$\begin{aligned} HRS &= \sin\left(\frac{2\pi \times HR}{24}\right), \quad HRC = \cos\left(\frac{2\pi \times HR}{24}\right), \\ DNS &= \sin\left(\frac{2\pi \times DN}{365.25}\right), \quad DNC = \cos\left(\frac{2\pi \times DN}{365.25}\right), \end{aligned} \tag{6.12}$$

where HRS, HRC, DNS, DNC are the sine and cosine components of HR and DN, respectively. In the previous NN model, there is only one more parameter, sunspot number (SSN), is added besides the HR and DN parameters [33]. The previous NN model is able to predict TEC at Chumphon station quite well compared to the IRI-2007 model. However, the previous model needs to be improved to reduce the error of TEC prediction. The suggested solution is including the magnetic activity parameter into the input of NN. Moreover, other solar proxies besides the sunspot number could improve performance of NN [27]. Thus, the improved NN model aims to extend the input space with additional solar activity and magnetic activity indices.

Besides SSN, the solar radio flux ($F_{10.7}$) represents the solar activity as well. The $F_{10.7}$ index measures the radiation from the solar at 2.8 GHz (10.7-cm wavelength). The daily SSN (ftp.ngdc.noaa.gov) and daily $F_{10.7}$ (www.ngdc.noaa.gov/nndc/struts) from January 2005 to March 2011 are plotted in Fig. 6.7. Both solar activity indices show the similar variation but not exactly the same. For instance, during the observational period, the $F_{10.7}$.reaches the maximum in January 2005 and March 2011 whereas the SSN reaches the maximum in July 2005. Therefore, both parameters are employed as the input of NN in order to improve the accuracy of TEC prediction. Due to the high fluctuation of daily indices degrading the efficiency of NN, the SSN and $F_{10.7}$ data are pre-processed by being center averaged over three days, one week (7 days), one solar rotation (27 days), and three solar rotations (81 days) [27], [33], [39].

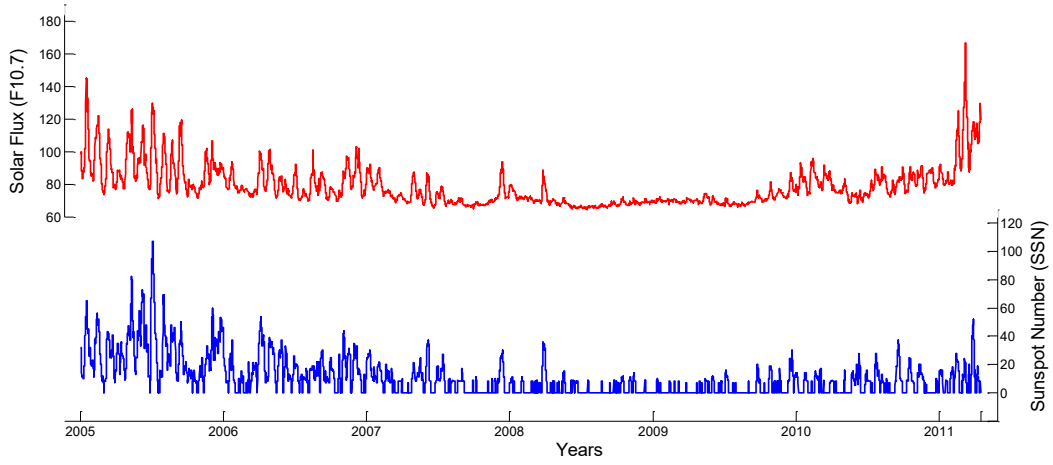

Figure 6.7: The observed $F_{10.7}$ and SSN from 1997 to 2007.[]

Two magnetic activity indices including equivalent planetary amplitude (Ap) and disturbance storm time (Dst) are also considered as the input parameters of NN. The Ap index

(ftp.ngdc.noaa.gov) measures the strength of disturbance in the earth's magnetic field while Dst index (http://wdc.kugi.kyoto-u.ac.jp/dst_realtime/) measures the equatorial magnetic disturbance. Since Ap and Dst are 3-hourly index and hourly index, respectively, the averaged data with a long period like 7 days, 27 days, or 81 days do not represent the variation very well. Therefore, Ap and Dst are only preprocessed to produce the 3-day-averaged data.

In short, there are 6 cases of input for the SSN and $F_{10.7}$ data including none-data, daily data, 3-day-averaged data, 7-day-averaged data, 27-day-averaged data, and 81-day-averaged data. While there are 3 cases of input for the Ap and Dst including none-data, daily data, and 3-day-averaged data. Totally, there are 324 possible combinations of the input set through the daily data and the various center-averaged data of solar and magnetic proxies.

6.3.3 Architecture of the improved NN

The set of input parameters and the number of nodes of the hidden layer are chosen based on the minimum RMSE. Figure 6.8 shows the best input sets in terms of RMSE corresponding to various numbers of nodes of the hidden layer from the training process. The RMSE steadily declines from 2.27 to 2.05 according to the case of 8-node hidden layer to the case of 20-node hidden layer. Then the RMSE remains stable around 2.05 from the case of 21-node hidden layer to the case of 28-node hidden layer. Hence, the NN model with 25-node hidden layer is selected as the model of this work due to the smallest error (RMSE=2.0461) and acceptable complexity. The input set of this selected NN model includes HRS, HRC, DNS, DNC, 81-day-averaged SSN, 7-day-averaged $F_{10.7}$, 3-day-averaged A_p, and 3-day-averaged Dst. As a result, architecture of the improved NN is represented in the schematic diagram in Fig. 6.9. The output of the improved NN model, namely TEC'_{pred}, is compared with the TEC_{meas} and the output of the previous NN model [33], TEC_{pred}, in terms of RMSE and normalized RMSE.

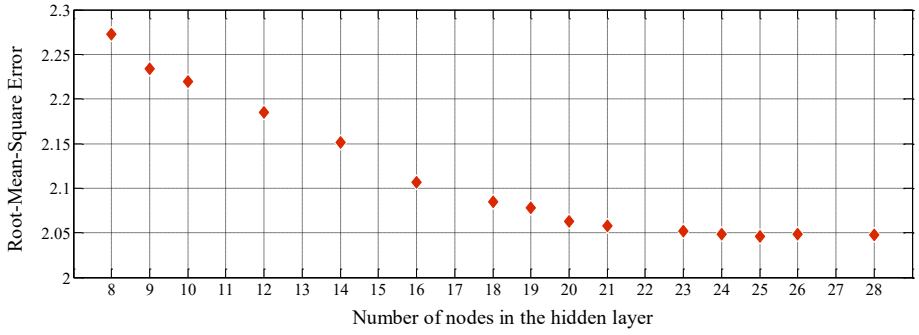

Figure 6.8. The smallest RMSE value of NN with 324 cases of input layer

and 8 to 30 nodes in the single hidden layer.

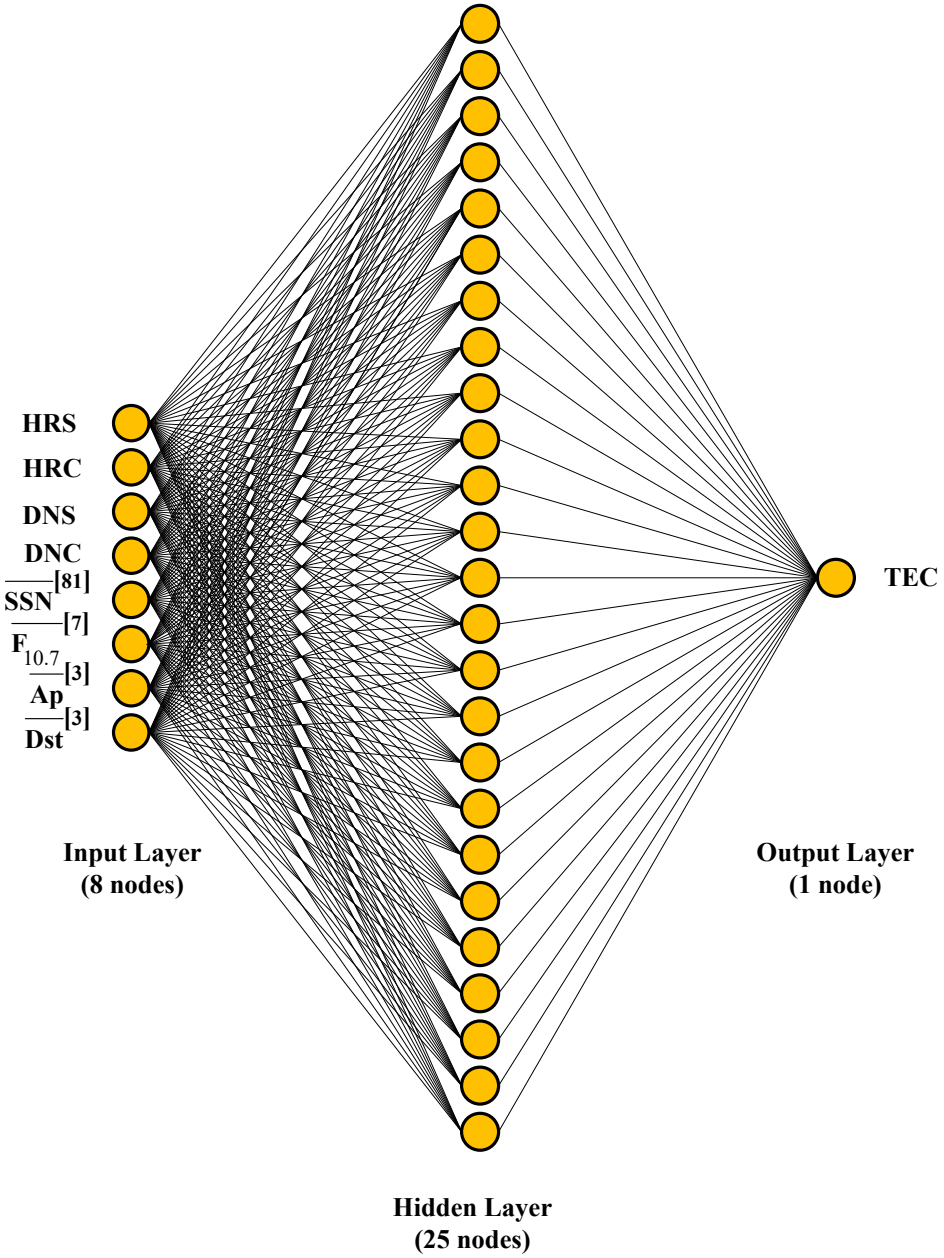

Figure 6.9. Schematic diagram of the improved NN model.

6.4. Results and discussions

6.4.1 Impact of the input parameters on the prediction

The input space of the improved NN model contains solar activity and magnetic activity indices: SSN, $F_{10.7}$, Ap, Dst. All four input parameters impact on the TEC variation which is related to the efficiency of NN. It is necessary to investigate the individual contribution

of these input parameters towards improving the TEC prediction. The improved NN model is trained by adding the input parameters one at a time with the data of the year 2005, 2006, 2008, 2009. Figure 6.10 shows the RMSE of the improved NN model for each input parameter included. In detail, when the SSN is firstly added to be an input of NN, the RMSE declines about 50% which is from 4.6978 to 2.3541. When the $F_{10.7}$ is continuously added to be an input of the NN, the RMSE declines about 5% which is from 2.3541 to 2.2389. Next, by adding the Ap to recent NN, the RMSE reduces about 6% which is from 2.2389 to 2.1000. When the final parameter, Dst, is added to the NN, the RMSE reduces about 4% which is from 2.1000 to 2.0270.

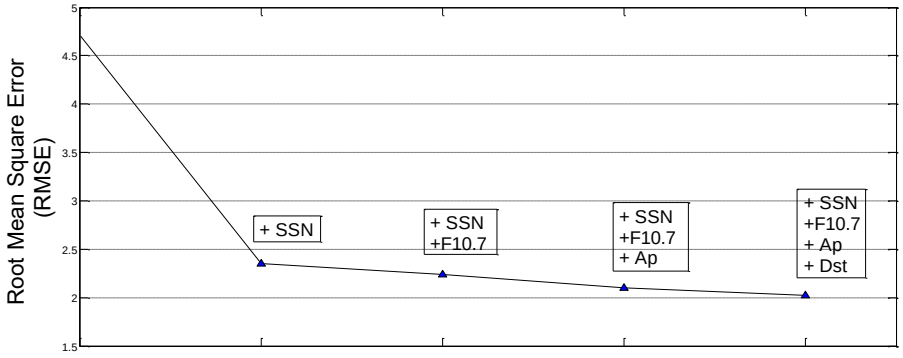

Figure 6.10 The RMSE of the improved NN model for each input parameter included.

6.4.2 Comparisons between the previous and the improved NN model

Previously, the previous NN model and the IRI-2007 model are evaluated by 6 comparisons with respect to the hourly comparison, seasonal comparison, daytime and nighttime comparisons. The results show the previous NN model performs the TEC prediction well compared to the IRI-2007 model [33]. In scope of this work, we focus on comparing the improved NN model and the previous NN model during 2007 as well as testing the improved NN model in 2010.

For hourly comparison, the improved NN model is compared with the previous NN model and the observational data on the equinox and solstice days in 2007 as shown in Fig. 6.11. Due to the loss of data on December 22, we make the comparison on December 25 as a December solstice. In this figure, the upper panel of each day plots the TEC'_{pred}, TEC_{pred}, and TEC_{meas} while the lower panel represents the errors of the improved NN model and the

previous NN model. The trend of predicted value of both previous and improved NN agrees well with the measured values with the minimum peak at pre-sunrise and the maximum peak at mid-day. In particular, the TEC_{pred} and TEC'_{pred} resemble the TEC_{meas} closely during the pre-sunrise period with the error approaching to zero. Besides that, TEC'_{pred} matches TEC_{meas} during the mid-day period on March 20 and the mid-night period on June 21. In addition, the prediction of previous NN and improved NN in the solstice days is better than the ones in the equinox days, the period with frequent occurrence of equatorial plasma bubble. The previous NN and the improved NN give the best prediction during December solstices with the normalized RMSE of 0.1056 and 0.1195, respectively. On the other hand, the previous NN model and improved NN model show the worst prediction during September equinox with the normalized RMSE of 0.2191 and 0.21, respectively. The detail of comparisons in terms of RMSE and normalized RMSE are shown in the Table 6.1. The improved NN model demonstrates lower RMSE and normalized RMSE than the previous model on March 20, June 21, and September 23. For overall year of 2007, the improved NN model with the averaged RMSE of 2.2241 and the normalized RMSE of 0.1482 predicts more precisely than the previous NN model with the averaged RMSE of 2.43 and the normalized RMSE of 0.1619. Hence, we can infer that the proposed model with the extended input space has improved the prediction ability.

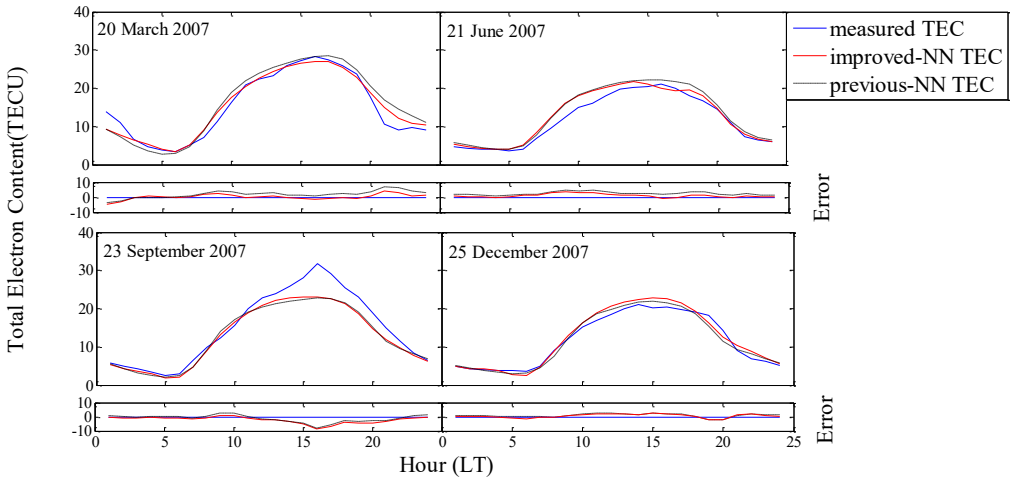

Figure 6.11: The measured TEC, improved-NN TEC and previous-NN TEC for the equinox and solstice days in 2007 over Chumphon station.

Table 6.1: The averaged measured TEC, RMSE and normalized RMSE of the improved NN model and the previous NN model for the equinox and solstice days in 2007 over Chumphon station.

Date	$\overline{\text{TEC}_{\text{meas}}}$	Root Mean Square Error		Normalized Root Mean Square Error	
		Improved NN	Previous NN	Improved NN	Previous NN
March 20	15.2145	1.7796	2.5750	0.1170	0.1692
June 21	11.8384	1.5967	1.8717	0.1349	0.1581
September 23	14.9391	3.1366	3.2726	0.2100	0.2191
December 25	11.7381	1.4022	1.2401	0.1195	0.1056
All year 2007	15.0113	2.2241	2.4300	0.1482	0.1619

For seasonal comparison, the predicted results of the improved NN model and the previous NN model are compared with each other during four distinct seasons including March equinox, June solstice, September equinox, and December solstice. The data for this comparison are monthly median values which were described in [33]. The Fig. 6.12 is the same as Fig. 6.11, except for season. Both hourly and seasonal comparisons have similar features with approximate shape of the predicted value of the previous and improved NN and the measured values. The predicted values of both the improved NN model and the previous NN model precisely match the TEC_{meas} during the comparison time. However, the TEC_{pred} and TEC'_{pred} slightly underestimate TEC_{meas} from 1030LT to 2330LT in March and September. The results in December solstice show the best performance of the previous NN model and the improved NN model with the normalized RMSE of 0.0448 and 0.0633, respectively. On the other hand, the previous NN and the improved NN show the worst prediction during March and September equinox with the normalized RMSE of 0.1253 and 0.1648, respectively. The RMSE and the normalized RMSE of both models for 12 months are compared in Table 6.2. The previous NN model performs better prediction in June, August, September, and December with

slightly smaller RMSE. Meanwhile, the improved NN model performs better prediction in the rest of year 2007. Especially, the RMSE of the improved NN model is twice less than the RMSE of the previous NN model in January, February, and July. In short, the proposed model predicts more precisely than the previous model for most of the months in 2007.

Table 6.2: The averaged measured TEC, RMSE and normalized RMSE of the improved NN model and the previous NN model for 12 months in 2007 over Chumphon station.

Month	$\overline{TEC_{meas}}$	Root Mean Square Error		Normalized Root Mean Square Error	
		Improved NN	Previous NN	Improved NN	Previous NN
January	14.2542	0.4161	0.8064	0.0292	0.0566
February	16.2201	0.4839	1.6276	0.0298	0.1003
March	18.1308	1.8756	2.2716	0.1034	0.1253
April	18.4332	1.6524	1.7156	0.0896	0.0931
May	15.6516	0.9199	1.0689	0.0588	0.0683
June	13.1770	1.0036	0.8331	0.0762	0.0632
July	13.2810	0.5285	1.3604	0.0398	0.1024
August	12.9961	0.6826	0.5585	0.0525	0.043
September	14.5920	2.4042	1.7339	0.1648	0.1188
October	15.1024	1.9649	1.9995	0.1301	0.1324
November	13.3732	0.9939	1.0870	0.0743	0.0813
December	12.2519	0.8129	0.5486	0.0663	0.0448

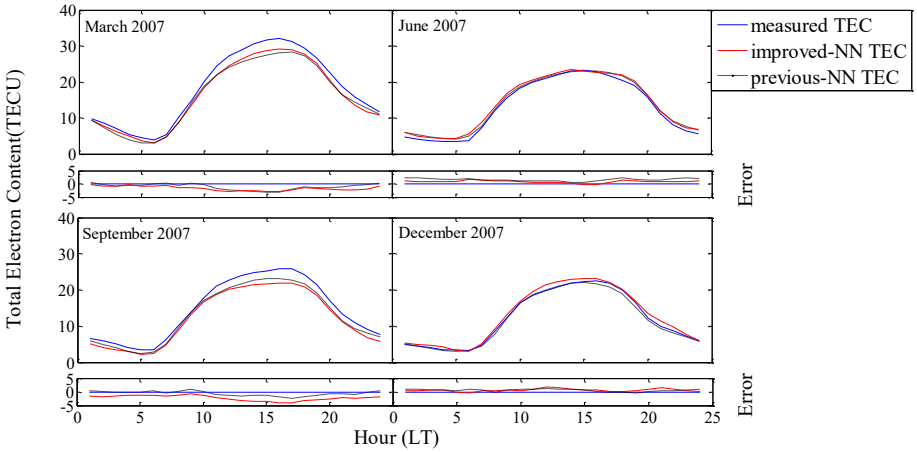

Figure 6.12: The measured TEC, improved-NN TEC and previous-NN TEC for the equinox and solstice months in 2007 over Chumphon station.

The 365-day variation of predicted and measured values at mid-night (0030LT), pre-sunrise (0630LT), mid-day (1230LT), and pre-sunset (1830LT) are compared to investigate the effect of daytime and nighttime to NN model as shown in Fig. 6.13. For mid-night comparison, both the previous NN model and the improved NN model predict the TEC over Chumphon station quite well with the normalized RMSE of 0.2510 and 0.2565, respectively. Similarly, for pre-sunrise comparison, although their RMSE is slightly higher than previous comparison, both models still keep the good prediction. In detail, the normalized RMSE of the previous NN model and the improved NN model are 0.3237 and 0.3424, respectively. The worst prediction of both models during nighttime may be a result of plasma bubble which always occur at nighttime and cause the drastic TEC variation. On the other hand, the previous NN model and the improved NN model perform the best prediction at daytime. The normalized RMSE of the previous NN model are 0.1202 for mid-day comparison and 0.1281 for pre-sunset comparison. While the normalized RMSE of the improved NN model are 0.1036 for mid-day comparison and 0.1124 for pre-sunset comparison. In general, as shown in Table 6.3, the improved NN model shows better prediction in mid-day and pre-sunset while the previous NN model shows better prediction in mid-night and pre-sunrise with slightly smaller RMSE.

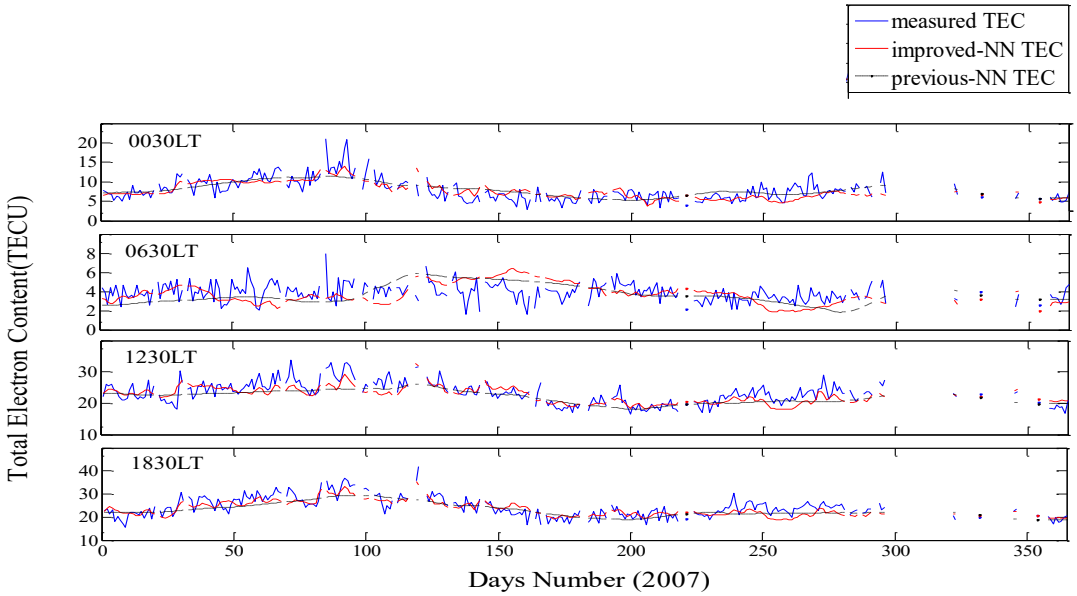

Figure 6.13: The measured TEC, improved-NN TEC, previous-NN TEC for mid-night (0030LT),pre-sunrise (0630LT), mid-day (1230LT), and pre-sunset (1830LT) in 2007 over Chumphon station.

Table 6.3: The averaged measured TEC and normalized RMSE of the improved NN model and the previous NN model for mid-night (0030LT), pre-sunrise (0630LT), mid-day (1230LT), and pre-sunset (1830LT) in 2007 over Chumphon station.

Time	$\overline{TEC}_{meas}$	Root Mean Square Error		Normalized Root Mean Square Error	
		Improved NN	Previous NN	Improved NN	Previous NN
0030LT	7.8826	2.0215	1.9788	0.2565	0.2510
0630LT	3.8696	1.3248	1.2525	0.3424	0.3237
1230LT	23.3038	2.4133	2.8003	0.1036	0.1202
1830LT	24.3282	2.7335	3.1166	0.1124	0.1281

6.4.3 Forecasting capability of the improved NN model

The improved NN model is tested in 2010 in order to evaluate its forecasting capability. As a result, we also compare the improved-NN TEC and measured TEC in respect of hourly comparison, seasonal comparison, daytime and nighttime comparisons.

For hourly comparison, the results of improved NN model are compared with observational data on equinox and solstice days in 2010 as shown in Fig. 6.14. In this comparison, December 28 is used as a December solstice instead of December 22 due to the loss of data. The improved NN model generally agrees with the measured value well but being almost underestimated. From the Table 6.4, it is evident that our model performs the best prediction on June solstice with the smallest normalized RMSE of 0.1051, whereas the error on September equinox is the highest with the normalized RMSE of 0.2475. The averaged RMSE and normalized RMSE of the year 2010 are 3.8829 and 0.2181, respectively. The $\overline{TEC_{meas}}$, computed by averaging all of the measured TEC values during the year 2010, is equal to 17.8065 TECU.

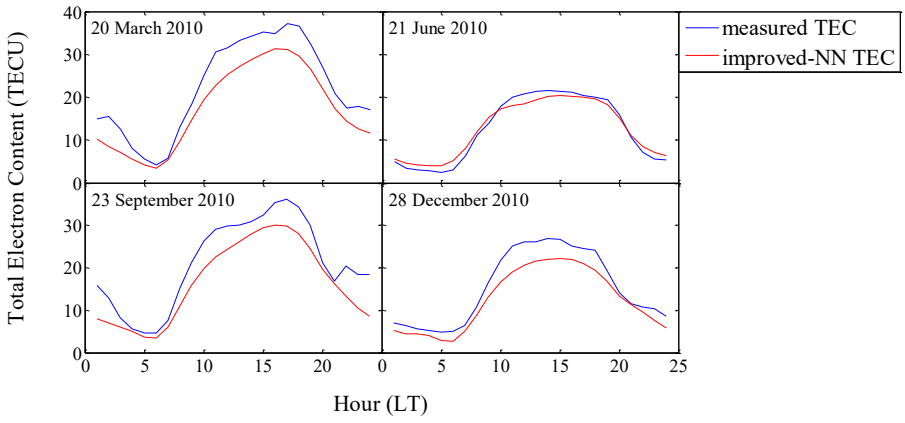

Figure 6.14: The measured TEC and improved-NN TEC for the equinox and solstice days in 2010 over Chumphon station.

Table 6.4: The averaged measured TEC and normalized RMSE of the improved NN model for the equinox and solstice days in 2010 over Chumphon station.

Date	$\overline{TEC_{meas}}$	Normalized Root Mean Square Error
March 20	22.0522	0.2263
June 21	13.0687	0.1051
September 23	21.0514	0.2475
December 28	15.3679	0.2174
All year 2010	17.8065	0.2181

In addition, we test the effective of the improved NN model during only quiet time with the weak geomagnetic storm. The geomagnetic storm is caused by the strong interaction between solar winds and the Earth's magnetosphere. The TEC increases during the first 24 hour of the storm and then declines below its quiet time value and recovers one or two days later [44]. The geomagnetic storm can be classified in range of Dst index [45] as shown in Table 6.5. The weak geomagnetic storm is defined as the Dst index in a range of (-50nT,-30nT). Therefore, the input space of the NN during the weak-geomagnetic-storm period is conducted by removing the time that Dst value is out of this range. Afterwards, this modified model is applied to see the real performance of NN without storm effect. Consequently, the NN model is able to predict well the TEC value due to the stability of plasma density. For the whole year 2010, the NN model during only the weak-geomagnetic-storm period has an averaged RMSE of 3.8591. It shows the slightly better performance than the NN including storm time which has an averaged RMSE of 3.8829 in 2010.

Table 6.5: The level of Geomagnetic storm according to range of DST index.

Dst	Level of Geomagnetic Storm
-50 nT $\leq$ Dst< -30 nT	Weak
-100 nT $\leq$ Dst< -50 nT	Moderate
Dst< -100 nT	Intense

For seasonal comparison, the results conducted in March, June, September, and December as shown in Fig. 6.15 are similar to the results of hourly comparison. The improved-NN TEC matches the measured TEC with the lowest normalized RMSE of 0.0737 in June and the highest normalized RMSE of 0.2492 in December. In particular, the results in June coincide closely with observational data for most of the time. The high RMSE in December can be simply explained by the lack of GPS data on some days leading to unsatisfactory prediction.

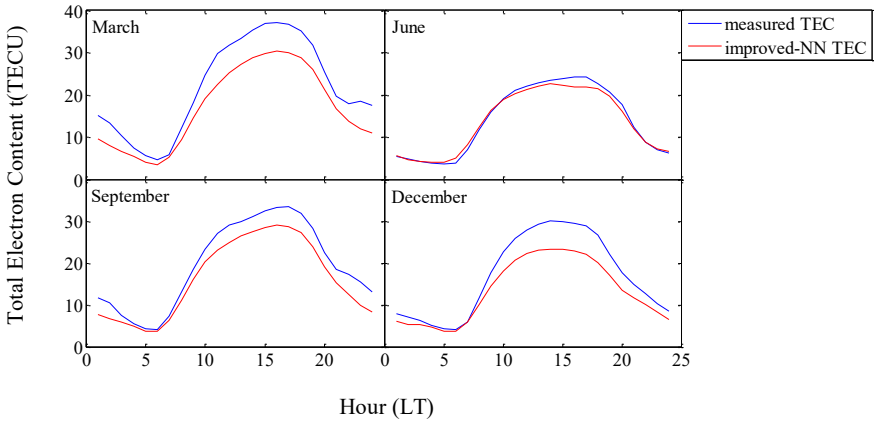

Figure 6.15: The measured TEC and improved-NN TEC for the equinox and solstice months in 2010 over Chumphon station

Table 6.6: The averaged measured TEC and normalized RMSE of the improved NN model for the equinox and solstice months in 2010 over Chumphon station.

Date	$\overline{\text{TEC}_{\text{meas}}}$	Normalized Root Mean Square Error
March	21.8526	0.2384
June	14.0544	0.0737
September	19.5359	0.1816
December	16.9726	0.2492

Moreover, we compare the predicted and measured values at mid-night (0030LT), pre-sunrise (0630LT), mid-day (1230LT), and pre-sunset (1830LT) in 2010. The improved NN model can predict TEC quite well during nighttime with the normalized RMSE of 0.3776 and

0.3124 for mid-night comparison and pre-sunrise comparison, respectively. In detail, the improved-NN TEC matches the measured TEC in February and May to August for mid-night comparison, and in July and August for pre-sunrise comparison. However, the improved NN model shows the best forecasting capability during daytime with the normalized RMSE of 0.1657 for mid-day comparison and the normalized RMSE of 0.1779 for pre-sunset comparison. The improved-NN TEC closely resembles the measured TEC especially in early and middle of the year 2010.

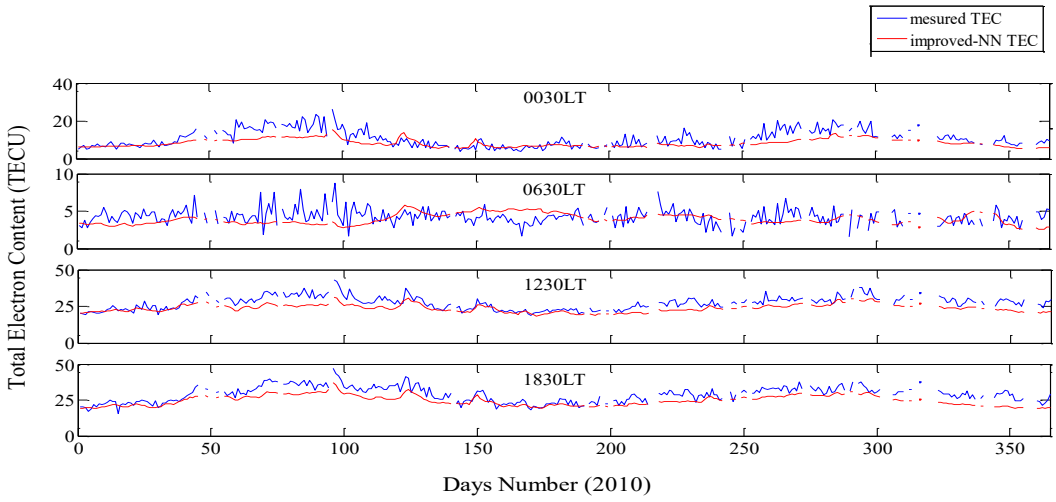

Figure 6.16: The measured TEC and improved-NN TEC for mid-night (0030LT), pre-sunrise (0630LT), mid-day (1230LT), and pre-sunset (1830LT) in 2010 over Chumphon station.

Table 6.7: The averaged measured TEC and normalized RMSE of the improved NN model for mid-night (0030LT), pre-sunrise (0630LT), mid-day (1230LT), and pre-sunset (1830LT) in 2010 over Chumphon station.

Date	$\overline{TEC}_{meas}$	Normalized Root Mean Square Error
0030LT	10.6405	0.3776
0630LT	4.2414	0.3124
1230LT	27.3125	0.1657
1830LT	28.7863	0.1779

6.5 Summary

An improved NN model for predicting and forecasting TEC over Chumphon station, Thailand is constructed. The input space is extended with parameters of SSN, $F_{10.7}$, A_p, Dst which are pre-processed by being center averaged. After a trial-and-error basis, the NN with 25 nodes of hidden layer is selected in our improved model. The NN is trained in 2005, 2006, 2008, and 2009, tested in 2007 and 2010. The performance of the improved NN model is evaluated by comparing to the previous model and the measured data. The results indicate that the improved model can predict the TEC well, especially in the solstice days as well as during noon time. Moreover, the improved NN model performs better prediction than the previous NN model as shown in several comparisons in 2007. The better performance of the improved model is due to its extended input space including solar activity and geomagnetic activity indices. In addition, the improved model is capable of forecasting TEC in 2010 well. Among the input parameters, $F_{10.7}$ has the most impact on the error of prediction of NN. In the future, we plan to extend the TEC data up to one solar cycle at Chumphon station and the other stations within Thailand in order to develop a reliable TEC modeling over this region.

Chapter 7

Conclusions

7.1 Summary

During the ionospheric irregularity periods, the plasma density drastically varies and results in several phenomena such as plasma bubble occurrences. It affects the GPS signal propagating along the satellite-receiver path. There are two typical effects including ionospheric delay and scintillations. The ionospheric delay due to the dispersive medium of the ionosphere contains the group delay and phase advance on GPS signal. At the receiver, it causes the error on GPS observations leading to the incorrect positioning. On the other hand, the scintillations cause the rapid fluctuations in terms of phase and amplitude of the GPS signal. In some cases, these fluctuations are especially too fast for the receiver to track the signal. Consequently, it can lead to the loss-of-lock and loss-of-signal in worth case. It affects the availability, precision, and reliability of the GPS signal which is increasingly important in our daily life, especially in applications related to human safety issue such as aeronautical navigation. Hence, it is necessary to study the ionosphere and its effects on the GPS signal.

In this thesis, the ionospheric scintillations are studied at Chumphon station, Thailand. The $S4$ index is derived from a L1 RF recorder by using the GPS software receiver. In order to compute the $S4$ index, there are two steps need to be done including detrending and ambient noise removal. We attempt to observe the $S4$ index on the day with plasma bubble occurrences due to its high possibility of serve scintillations occurrences. As a result, the strong scintillations which the $S4$ is greater than 0.5 are observed in several visible GPS satellites.

The scintillation can lead to the loss of phase lock at the GPS receiver. Thus, in the scope of this thesis, we also present the loss-of-lock statistics at KMITL station near the Suvarnabhumi airport, Thailand. The loss-of-lock is derived from the RINEX file obtained from the GPS dual frequency receiver. The probability of loss-of-lock is computed to analyze the loss-of-lock statistics. The results show that the L_2 frequency is more susceptible to the loss-of-lock events than the L_1 frequency. The results also show the relationship between the loss-of-lock and ROTI and the elevation angles.

Moreover, we develop an improved TEC modeling at Chumphon station, Thailand. The TEC is one of the essential parameters for characterizing the plasma density variation of the ionosphere. The TEC model in Thailand acts as a local model which is necessary for studying the ionospheric irregularities over the EIA region. The neural network with a capability of estimating the non-linear data is employed for this TEC model. The input space is extended from the one of previous model with the solar activity and magnetic activity indices including SSN, $F_{10.7}$, A_p, and Dst. The NN is trained in 2005, 2006, 2008, and 2009, tested in 2007 and 2010. The results show that the improved NN model can predict the TEC more precisely than the previous NN for most of the months in 2007. The improved NN model also performs well the TEC prediction in 2010.

7.2 Future Works

The scintillations computation and loss-of-lock statistics are studied in this thesis. The scintillations are probably a reason of loss-of lock occurrences due to the high fluctuation of GPS signal in terms of phase and amplitude. However, the scintillations are not the only mechanism causing the loss of phase lock at receiver. There are the other causes such as multipath and shadowing. Hence, investigating a relationship between scintillations and loss-of-lock occurrences is also interesting issue. In the future, we plan to observe the scintillations and loss-of-lock at several stations in SEALION project and study the correlation between the scintillations and loss-of-lock over the EIA region.

For TEC modeling project, we need to improve the performance of the neural network for the incoming solar maximum period. Therefore, the neural network should be trained for a longer period which covers at least one solar cycle. Moreover, the available GPS data for several stations in SEALION project is a motivation for producing a local TEC map based on neural network. This map is useful for studying the ionospheric phenomena such as plasma bubble moving, ionospheric storm moving over the EIA region.

REFERENCES

[1] “Effect of Ionospheric Scintillations on GNSS – A White Paper,” SBAS Ionospheric Working Group, 2010.

[2] http://wdc.nict.go.jp/IONO2/SEALION.

[3] Tsugawa, T., “Observational Studies on Large-Scale Traveling Ionosphere Disturbances Using GPS Receiver Networks,” Ph.D. dissertation, Kyoto university, 2004.

[4] Brown, B., “HF Propagation tutorial,” [Online]. Available: http://www.astrosurf.com/luxorion/qsl-hf-tutorial-nm7m3.htm.

[5] Davies, K., “Ionospheric Radio,” IEE Electromagnetic Waves Series, Peter Peregrinus Ltd, vol. 31, 1990.

[6] Knight, M. F., ‘Ionospheric Scintillation Effects on Global Positioning System Receivers,” Ph.D. dissertation, The University of Adelaide, 2000.

[7] http://sidc.oma.be/.

[8] http://www.ips.gov.au/.

[9] Kintner, P., Humphreys, T., Hinks, J.,“GNSS and Ionospheric Scintillation How to Survive the Next Solar Maximum,” Inside GNSS, July-Aug 2009.

[10] Larson, Axerald, “ASEN 5090 LECTURES NOTES,” Available online at: http://www.colorado.edu/ASEN/asen5090/.

[11] Seeber, G., “Satellite Geodesy: Foundations, Methods & Applications,” Walter de Gruyter, Berlin, New York, pp. 531, 1993.

[12] Ma, G., and Maruyama, T., “Derivation of TEC and estimation of instrumental biases from GEONET in Japan,” Ann. Geophys., vol. 21, pp. 2083-2093, 2003.

[13] Akos, D., “A Software Radio Approach to Global Navigation Satellite System (GNSS) Receiver Design,” Ohio University, 1997.

[14] Theodore, L., B., Paul, M., K., "Development and Use of a GPS Ionospheric Scintillation Monitor," IEEE Transactions on Geoscience and Remote Sensing, vol. 39, no.5, 2011.

[15] Van Dierendonck, A., J. Klobuchar, Q. Hua, "Ionospheric scintillation monitoring using commercial single frequency C/A code receivers," Proc. ION GPS, p1333-1342, Salt lake City, UT., Sept. 1993.

[16] Borre, K., Akos, D., Bertelsen, N., Rinder, P., Jensen, S., "A Software Defined GPS and Galileo Receiver: Single-Frequency Approach," Birkhäuser, Boston, MA, 2006.

[17] Falletti, E., Pini, M., and Presti, L., "Low Complexity Carrier-to-Noise Ratio Estimators for GNSS Digital Receivers," IEEE Transactions on Aerospace and Electronic Systems, Vol.47, No.1, pp. 420-437, January 2011.

[18] Pullen, S., Lee, J., and Luo, M., "Ephemeris Protection Level Equations and Monitor Algorithms for BAS," Proceedings of the 14th International Technical Meeting of the Satellite Division of the Institute of Navigation (ION GPS 2001), pp. 1738-1749, 2001.

[19] "Resolution for ionospheres issues in implementing GNSS," Working paper, CNS/MET SG/14 – WP/43, 19 July 2010.

[20] Gurtner, W., Mader, G., Arthur, D., "A Common Exchange Format for GPS Data," CSTG GPS Bulle-tin Vol.2 No.3, May/June 1989.

[21] Gurtner, W., "RINEX: The Receiver Independent Exchange Format Version 2.10," June 2001.

[22] Spofford, P.R., Remondi, B.W., "The National Geodetic Survey Standard GPS Format SP3," www.ngs.noaa.gov/orbits/.

[23] http://133.243.237.146/IONO2/THAI-GPS/CPN/ROTI/.

[24] Hernandez-Pajares, M., Juan, J., Sanz, J., "Neural network modeling of the ionospheric electron content at global scale using GPS," Radio Sci. 32, pp. 1081–1090, 1997.

[25] Bilitza, D., "International Reference Ionosphere 2000," Radio Sci. 36 (2), 261–275, 2001.

[26] Tulunay, E., Senalp, E.T., Radicella, S.M., Tulanay, Y., "Forecasting total electron content maps by neural network technique," Radio Sci. 41, doi: 10.1029/2005RS003285, 2006.

[27] Maruyama, T., "Regional reference total electron content model over Japan based on neural network mapping techniques," Ann. Geophys., vol. 25, pp. 2609–2614, 2007.

[28] Bhuyan, P. K., Barah, R. R., "TEC derived from GPS network in India and comparison with the IRI," J. Adv. Space Res., vol. 39, pp.830-840, 2007.

[29] Xenos, T.D., Kouris, S.S., Casimiro, A., "Time-dependent prediction degradation assessment of neural-networks-based TEC forecasting models," Nonlinear Proc. Geophys., vol. 10, pp. 585–587, 2003.

[30] Leandro, R.F., Santos, M.C., "A neural network approach for regional vertical total electron content modeling," Stud. Geophys. Geod., vol. 51 (2), pp. 279–292, 2007.

[31] Habarulema, J.B., McKinnell, L.A., Cilliers, P.J., "Prediction of global positioning system total electron content using neural networks over South Africa," J. Atmos. Solar Terrest. Physics., vol. 69(15), pp. 1842–1850, 2007.

[32] Acharya, R., Roy, B., Sivaraman, M.R., Dasgupta, A., "Prediction of ionospheric total electron content using adaptive neural network with in-situ learning algorithm," Adv. Space Res., vol. 47(1), pp. 115-123, 2011.

[33] Watthanasangmechai, K., Supnithi, P., Lerkvaranyu, S., Tsugawa, T., Nagatsuma, T., Maruyama, T., "TEC prediction with neural network for Thailand equatorial latitude station. Earth Planets Space," *in press.*

[34] Bilitza, D., "A correction for the IRI topside electron density model based on Alouette/ISIS topside sounder data," Adv. Space Res., vol. 33(6), pp. 838–843, 2004.

[35] Haykin, S., "Neural Networks, A Comprehensive Foundation," Macmillan College Publishing Company, 1994.

[36] Fausett, L., "Fundamentals of Neural Networks; Architectures Algorithms and Applications," Prentice-Hall, Inc., New Jersey, 076324, 1994.

[37] Rumelhart, D. E., Hinton, G. E., and Williams, R. J., "Learning representations by back-propagating errors," Nature., vol. 323, pp. 533–536, 1986.

[38] Sarma and T. Madhu., "Modelling of foF2 using neural networks at an equatorial anomaly station," Current Sci., vol. 89(7), pp. 1245–1247, 2005.

[39] Nakamura, M.I., Maruyama, T., Shidama, Y., “Using a neural network to make operational forecasts of ionospheric variations and stroms at Kokubunji, Japan,” Earth Planets Space, vol. 59, pp. 1231–1239, 2007.

[40] Hagan, M.T., Demuth, H.B., Beale, M.H., “Neural Network Design,” PWS Publishing Company, 1996.

[41] Otsuka, Y., Ogawa, T., Saito, A., Tsugawa, T., Fukao, S., Miyazaki, S., “A new technique for mapping of total electron content using GPS network in Japan,” Earth Planets Space., vol. 54, pp. 63–7, 2002.

[42] Williscroft, L.-A., Poole, A.W., “Neural Networks, foF2, sunspot number and magnetic activity,” Geophys. Res. Lett., vol. 23 (24), pp. 3659–3662, 1996.

[43] Poole, A.W., McKinnell, L.-A. On the predictability of foF2 using neural networks. Radio Sci., vol. 1, pp. 225–234, 2000.

[44] Yamamoto, A., Ohta, Y., Okuzawa, T., Taguchi, S., Tomizawa, I., and Shibata, T., ”Characteristics of TEC variations observed at Chofu for geomagnetic storms,” Earth Planets Space, vol.52, no.11, pp.1073-1076.

[45] Kamide, Y., Yokoyama, N., Gonzales,W., Tsurutani, B.T., Daglis, I.A., Brekke, A., Masuda, S., “Two-step development of geomagnetic storms,” J. Geophys. Res., vol. 103A (4), pp. 6917–6921, 1998.

APPENDIX

LIST OF PUBLICATIONS

Journal (Preparation/ Submission/Review Process)

1. **P.L.H. Phong**, K. Watthanasangmechai, P. Supnithi, T. Nagatsuma, T. Tsugawa and T. Maruyama, "TEC Modeling Based on Improved Neural Network over Chumphon station, Thailand," **Journal of Advanced Space Research.** *(Revision)*

Conference Proceedings

1. **P.L.H. Phong**, S. Rungraengwajiake, and P. Supnithi, " Loss-of-Lock Statistics from the GPS Receiver Near Suvarnabhumi Airport, Thailand," 2011 IEEE International Conference on Space Science and Communication (IconSpace), 12-13 July 2011, Penang, Malaysia.
2. K. Watthanasangmechai, **P.P.L. Hoai**, and P. Supnithi," TEC modeling based improved neural network over Chumphon," International Reference Ionosphere (IRI) 2011Workshop, Hermanus, South Africa, Oct. 10-14, 2011.
3. **P.L.H. Phong**, P. Supnithi, T. Tsujii, " Ionospheric Scintillation Monitoring using software GPS receiver at Chumphon station, Thailand," The first AOSWA (Asia-Oceania Space Weather Alliance) Workshop, Chiang Mai, Thailand, Feb. 22-24, 2012.
4. **P.L.H. Phong**, P. Supnithi, T. Tsujii, " Ionospheric Scintillation Monitoring using software GPS receiver at Chumphon station, Thailand," The 27th International Technical Conference on Circuits/Systems, Computers and Communications (ITC-CSCC 2012), Sapporo, Japan, July 15-18, 2012.